High-resolution X-ray spectroscopy of Warm-Hot Baryons in Intergalactic Medium

Jussi Ahoranta

ACADEMIC DISSERTATION

Department of Physics
Faculty of Science
University of Helsinki
Helsinki, Finland

To be presented, with the permission of the Faculty of Science of the University of Helsinki, for public criticism in in auditorium E204, Physicum (Gustav Hällströmin katu 2), on April 14th 2023.

Helsinki 2023

Abstract

This dissertation focuses on observational research of diffuse, highly ionized intergalactic gas that populates the dark–matter dominated large–scale structure of the Universe. Such intergalactic medium is expected to be the most important reservoir of cosmic baryons, yet studying it observationally is challenging due to its hot temperature ($T \sim 10^5 - 10^7$ K), high ionization states (so that signals are produced mainly in UV/X–ray bands) and low number densities of metal ions. Therefore observational information on the evolution, state and the distribution of the cosmic baryons is currently limited, and our understanding on these matters rely heavily on the information yielded by cosmological, hydrodynamical simulations. The goal of the research included in this work was to improve this situation by producing new, observation–based information on X–ray emitting/absorbing diffuse cosmic structures.

The soft X–ray band is especially suitable for studying the diffuse intergalactic medium because it covers the energy range that can trace the most important spectral lines produced by the hot ($T \sim 10^6$ K) gas phases. Generally this also means that the X–ray band is sensitive to signals other than those measurable at FUV/EUV –bands, which instead yield information on the cooler gas phases ($T \sim 10^5$ K or less). Whereas the focus of my PhD research is on soft X–ray band high energy resolution studies, the X–ray band picture is complemented with relevant information on UV –band/simulations whenever such information is available. Indeed, even small additional observational information obtained at one of these bands can have significant scientific value when considered properly with the relevant data available at the other.

The topics of the presented research papers range from mesurements of the intra–cluster/–group medium (ICM/IGM) physical properties to those of the warm–hot intergalactic medium (WHIM). We publish several astrophysically noteworthy measurement results, including the first detections of line emission (O VII) from cooled gas

($kT \lesssim 0.5$ keV) in IGM/ICM environment of individual objects, the first measurement results on asymmetric velocity fields in intra–group medium, and two possible discoveries of multiphase WHIM absorbers, both of which appear to be associated to filamentary galaxy large scale structures. In general, our results seem to draw somewhat more variegated picture on the inter–galactic gas than one might have expected beforehand: our observational studies indicate existence of complex multiphase structures and gas dynamics in ICM/IGM environments, while our WHIM studies imply that multiphase structures are common also in filamentary WHIM. These outcomes were achieved through combination of extensive exploration of archival data and by use of novel type of analysis methods that I developed as a part of the work.

The thesis is structured as follows: in the first half of the introductionary section I give a broad picture on the research field and on the open questions within it, introduce (some of the) newly developed analysis methods that are utilized in the presented papers, and present the current high energy resolution spectrographs (Chapters 1-3). In the latter half of the introductionary section (Chapters 4-6), I discuss the future instruments relevant to our research, the methods availing the physical interpretation of X–ray spectral analysis results, and give short summaries of the included research papers. In the printed form of this thesis, the introductionary section is followed by copies of the original research papers.

Acknowledgements

List of publications

Publications included in this thesis

Paper I: (Ahoranta, Finoguenov, Bonamente et al. 2021)
J. Ahoranta, A. Finoguenov, M. Bonamente, S. Muzahid, N. Wijers, E. Tilton and J. Schaye, *Discovery of a multiphase O VI and O VII absorber in the circumgalactic/intergalactic transition region*, A&A, vol. 656, pp. A107, December 2021

Paper II: (Ahoranta, Nevalainen, Wijers et al. 2020)
J. Ahoranta, J. Nevalainen, N. Wijers, A. Finoguenov, M. Bonamente, E. Tempel, E. Tilton, J. Schaye, J. S. Kaastra and G. Gozaliasl, *Hot WHIM counterparts of FUV O VI absorbers: Evidence in the line-of-sight towards quasar 3C 273*, A&A, vol. 634, pp. A106, February 2020

Paper III: (Nevalainen, Tempel, Ahoranta et al. 2019)
J. Nevalainen, E. Tempel, **J. Ahoranta**, L. J Liivamägi, M. Bonamente, E. Tilton, J. S. Kaastra, T. Fang, P. Heinämäki, E. Saar and A. Finoguenov, *To be or not to be: the case of the hot WHIM absorption in the blazar PKS 2155-304 sight line*, A&A, vol. 621, pp. A88, January 2019

Paper IV: (Ahoranta, Finoguenov, Pinto et al. 2016)
J. Ahoranta, A. Finoguenov, C. Pinto, J. S Sanders, J. S Kaastra, J. de Plaa and A. C. Fabian, *Observations of asymmetric velocity fields and gas cooling in the NGC 4636 galaxy group X-ray halo*, A&A, vol. 592, pp. A145, August 2016

Paper V: (Pinto, Fabian, Werner et al. 2014)
C. Pinto, A. C. Fabian, N. Werner, P. Kosec, **J. Ahoranta**, J. de Plaa, J. S. Kaastra, J. S. Sanders, Y. Y. Zhang and A. Finoguenov, *Discovery of O VII line emitting gas in elliptical galaxies*, A&A, vol. 572, pp. L8, December 2014

Publications not included in this thesis

G. Gozaliasl, A. Finoguenov, H. G. Khosroshahi, C. Laigle, C. C. Kirkpatrick, K. Kiiveri, J. Devriendt, Y. Dubois, and J. Ahoranta, *Kinematic unrest of low mass galaxy groups*, A&A, vol. 635, pp. A36, March 2020

G. Gozaliasl,A. Finoguenov, M. Tanaka, K. Dolag, F. Montanari, C. Kirkpatrick, C. Charles, E. Vardoulaki, H. G. Khosroshahi, M. Salvato, C. Laigle, H. J. McCracken, O. Ilbert, N. Cappelluti, E. Daddi, G. Hasinger, P. Capak, N. Z. Scoville, S. Toft, F. Civano, R. E. Griffiths, M. Balogh, Y. Li, J. Ahoranta, S. Mei, A. Iovino, B. M. B. Henriques, and G. Erfanianfar, *Chandra centres for COSMOS X-ray galaxy groups: differences in stellar properties between central dominant and offset brightest group galaxies*, MNRAS, vol. 483, pp. 3545, March 2019

J. de Plaa, J. S. Kaastra, N. Werner, C. Pinto, P. Kosec, Y.-Y. Zhang, F. Mernier, L. Lovisari, H. Akamatsu, G. Schellenberger, F. Hofmann, T. H. Reiprich, A. Finoguenov, J. Ahoranta, J. J. Sanders, A. C. Fabian, O. Pols, A. Simionescu, J. Vink, H. Böhringer, *CHEERS: The chemical evolution RGS sample*, A&A, vol. 607, pp. A98, November 2017

M. Bonamente, J. Ahoranta, E. Tilton, E. Tempel and A. Morandi *Characterization of the warm-hot intergalactic medium near the Coma cluster through high-resolution spectroscopy of X Comae*, MNRAS, vol. 469, 4, pp. 3984, August 2017

C. Pinto, A. C. Fabian, A. Ogorzalek, I. Zhuravleva, N. Werner, J. Sanders, Y.-Y. Zhang, L. Gu, J. de Plaa, J. Ahoranta, A. Finoguenov, R. Johnstone and R. E. A. Canning, *Insights into the location and dynamics of the coolest X-ray emitting gas in clusters of galaxies* MNRAS, vol. 461, 2, pp. 2077, September 2016

C. Pinto, J. S. Sanders, N. Werner, J. de Plaa, A. C. Fabian, Y.-Y. Zhang, J. Kaastra, A. Finoguenov, and J. Ahoranta *Chemical Enrichment RGS cluster Sample (CHEERS): Constraints on turbulence*, A&A, vol. 575, pp. A38, March 2015

N. Beev, M. Kiviranta, J. van der Kuur, M. Bruijn, O. Brandel, S. Linzen, L. Fritzsch, J. Ahoranta, J. Penttilä, and L. Roschier, *Cryogenic time-domain multiplexer based on SQUID arrays and superconducting/normal conducting switches*, JPCS, pp. 507, May 2014

J. Ahoranta, M. Uunila, J. Huovelin, H. Andersson, R. Vainio, A. Virtanen and H. Kettunen, *Radiation hardness studies of CdTe and HgI$_2$ for the SIXS particle detector on-board the BepiColombo spacecraft*, NIM-A, vol. 605, pp. 344, July 2009

Contents

1 Background

The soft X–ray band ($\approx$ 250 eV–5 keV, or 2.5–50 Å) measurement devices provide opportunities to study hot, highly–ionized X–ray emitting/absorbing gas, which is highly abundant in the Universe, yet poorly undestood. Moderate energy–resolution devices with imaging capabilities can be used to investigate spatial distribution, temperatures, composition and other properties of such gas, whereas high energy resolution X–ray spectroscopy can yield direct, atomic level information on the physical states of the hot gas phases. Therefore, detailed studies on the X–ray band, combined with the relevant information from other bands of the electromagnetic spectrum, are capable to provide important pieces of information to fill up some of the gaps in our understanding of the Universe, its evolution, and the structures it contains.

1.1   The Big picture

Based on our current knowledge, the energy budget of the present–day Universe is dominated by three main components; dark energy (69 %), dark matter (26 %) and baryonic matter (5 % of the total energy density) [Planck Collaboration et al., 2014]. Whereas the two 'dark' components dominate the energy balance of the Universe, as it stands, they can be examined only indirectly, e.g., by studying their gravitational influence on the flows of baryonic matter and/or electro-magnetic radiation through the space. Such observational evidence suggests that the distribution of dark energy could be explained by a uniform gravitationally repulsive field, which ultimately gives rise to the accelerating expansion rate of the Universe that took over cosmologically recently [Riess et al., 1998, Perlmutter et al., 1999]. In contrast, the spatial distribution of dark matter is more intricate; Observational data and cosmological simulations indicate that the distribution of the dark matter forms a large scale, three dimensional web–like structure that fills the observable Universe [e.g., Gott et al., 1986, Schaye et al., 2015, Umehata et al., 2019, Bacon et al., 2021]. In this so–called cosmic–web, the most massive dark matter concentrations, seeded by the

primordial fluctuations in the Early Universe, connect to each other by thread–like dark matter filaments (as illustrated in the left half of Fig.1.1). This dark matter large scale structure dominates the distribution of the baryonic matter as well.

Within the present Universe, the baryons can exist in any of the four fundamental states: solid, liquid, gas, or ionized plasma. However, since the first three of these phases can only occur under strictly limited thermophysical conditions, almost all ($\gtrsim$ 99 %) of the cosmic baryons exist in the form of ionized plasma. Over the whole observable Universe, only a small fraction of hot, ionized gas is locked into gravitationally collapsed objects, such as stars or galaxies ($\approx$ 10 %), while majority of the baryons are expected to be found in diffuse media within the inter–galactic space. In taxonomic terms, the most important reservoir of cosmic baryons is the warm–hot intergalactic medium (from hereon, WHIM). The WHIM refers to intergalactic gas other than that filling the galaxy clusters (i.e., the intra–cluster medium, from here on ICM) or galaxy groups (the intra–group medium, IGM), but resides in the filamentary parts of the cosmic web (see the right half of Fig.1.1).

1.2   Observational status of the WHIM

During the past few decades, the existence and properties of WHIM have been studied intensively both observationally and through hydrodynamical simulations [e.g, Savage et al., 2011, Fang et al., 2012, Hussain et al., 2015, Pachat et al., 2016, Bonamente et al., 2016, Nicastro et al., 2018, Ahoranta et al., 2019, Kovacs et al., 2019, Wijers et al., 2019, Ahoranta et al., 2021, Tuominen et al., 2021, among others]. At high redshifts, a bulk of WHIM has been successfully detected in a photoionized (warm) phase that gives rise to the Lyα forest [Seljak et al., 2005]. At low redshifts, the baryons detected to date are either in the Lyα forest (approximately 20%, Penton et al. 2000) or in other phases that include collapsed objects. First measurements of electron column densities using localized fast radio bursts are consistent with the bulk of baryons at low redshifts being in the ionized state [Macquart et al., 2020], therefore implying that about half of the low–redshift baryons have not been understood, an issue also known as the missing baryons problem (see Figure 1.2). Cosmological, hydrodynamical simulations predict that the missing baryons in WHIM have been shock–heated to temperatures $\log_{10} T(K) =$5–7 [e.g., Davé et al., 2001, Cen and Ostriker, 1999], and that they locate in galaxy–sized halos and large–scale sheets and filaments [e.g. Nelson et al., 2018, Wijers et al., 2019]. The WHIM is expected to be characterized with very low number–densities (e.g., $\log_{10}(n_{\rm H}/{\rm cm}^{-3}) \approx -7 - -4$) and sub-Solar metallicites (FUV studies imply $Z \lesssim 0.1 \times {\rm M}_\odot$), although there are indica-
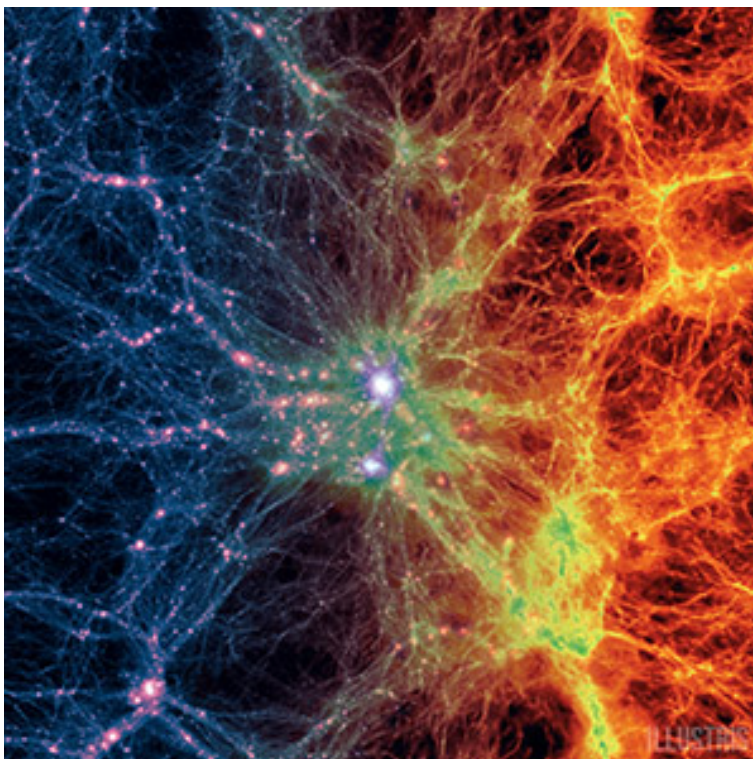
Figure 1.1: IllustrisTNG [Nelson et al., 2019] simulated, 15 Mpc/h slice of the cosmic web in the $z = 0$ universe. The left half of the picture shows the spatial distribution of dark matter (blue colour) along with that of galaxies (bright spots). The right half shows the predicted distribution of WHIM (filaments) and intracluster ('knots') gas; the hot gas phase is marked with green colour, whereas the yellow/orange shades correspond to warm/cool gas. The bright extended source in the center of the figure, where the various filamentary structures connect, is the most massive galaxy cluster within this slice. Credit: Illustris Collaboration

tions that the hot WHIM phases might have somewhat higher metallicities than the warm ones (J. Schaye, private communication; see also Martizzi et al. 2019 and the discussions in Ahoranta et al. 2021).

Due to low emission of diffuse, low n_i gas, the WHIM is more easily detectable through absorption studies (as discussed in more detail in Chapter 2). As it stands, quantitative FUV–band measurements of the warm WHIM phase ($\log_{10} T/\mathrm{K} \approx 5-6$) absorbers have enabled estimations on the amount of baryons associated to this phase. In contrast, the hot WHIM phase ($\log_{10} T/\mathrm{K} \approx 6-7$) that is mainly detectable in X–ray band remains poorly observed. This is presumably due to differences in observational instruments' sensitivities to measure weak WHIM signals at different bands: the warm WHIM phase produces the strongest signals in FUV band (e.g., H I , O VI line absorption), while the hot phase signal is strongest in the soft X-ray band (e.g., O VII – O VIII absorption). Considering the relative performance levels of present X–ray and FUV spectrographs, one requires two order of magnitudes higher ionic surface density for X–ray detection as compared to the FUV band. In practice, this means that in X–ray, one can only detect the strongest hot WHIM absorbers [as discussed, e.g., in Wijers et al., 2019, Ahoranta et al., 2021]. The main motivation of the WHIM research presented in this work (Papers I-III) was to improve the observational status of the hot WHIM phase.

1.3   Observing the baryons in ICM/IGM

The second most important reservoir of baryons is the inter–galactic medium within the galaxy clusters and groups. Galaxy clusters are the largest gravitationally bound objects in the Universe and the basic building blocks of the cosmic–web structure (Fig. 1.1). A single galaxy cluster consists of hudreds to thousands of individual luminous galaxies (and even larger number of dwarf galaxies) that are embedded inside a massive dark matter halo that can extend over several Mpc radial distances from the center of the system. Whereas the total masses of galaxy clusters range between 10^{14}–10^{15} M$_\odot$, about 80–85 % of their total mass is due to dark matter, a few per cent from galaxies, while the rest is in a form of highly–ionized, hot baryonic gas filling the intra–cluster space (i.e., the ICM). The ICM is characterized with ion temperatures ranging from sub–keV ($\log_{10} T/\mathrm{K}\sim 6$) to tens of keVs ($\log_{10} T/\mathrm{K}\sim 8$) with temperature increasing towards the outer parts. The galaxy groups, on the other hand, is a class of physically similar systems but with smaller total mass and a smaller number of galaxies.

Even in the most simplistic case of closely spherically symmetric, relaxed galaxy
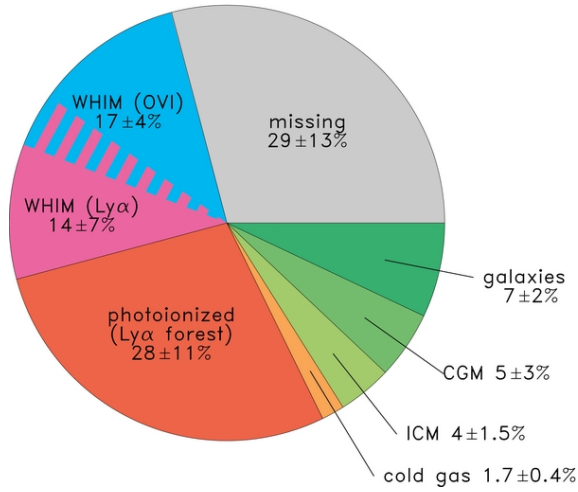
Figure 1.2: The baryon cencus in the local Universe as illustrated in Shull et al. [2011]. The missing sector is expected to contain dominantly warm/hot gas that is currently undetected due to its weak spectral signal.

clusters, the modeling the cold dark matter (CDM) haloes radial density distributions has been found to require an adoption of 'cusp models', such as the well known NFW–model [Navarro et al., 1996]. In this model, the CDM density scales as $\rho_{\mathrm{CDM}} \propto \rho_0 \, r^{-1}$ near the core of the halo and $\propto \rho_0 \, r^{-3}$ at the outer parts. Here, ρ_0 is a normalization parameter, whereas the transition between the models takes place at the so–called scale radius, R_s. Empirical studies have shown that the scale radius vary from halo to halo, ranging from sub–Mpc to Mpc distances [e.g., Voigt and Fabian, 2006]. Indeed, the numerical values of both ρ_0 and R_s are completely system specific. Effectively, the CDM gravity wells allow high baryon overdensities to form into cluster core regions that, in turn, give rise to efficient bremmstrahlung and line emission in X–ray. For the nearby objects, this signal is easily detectable with the current instrumentation. Due to exceptionally large size of these objects, measurable ICM/IGM emission signals of certain low–z objects extends over tens of arcmins in diameter on the sky plane.

Spectral analysis of the X–ray emission of nearby clusters/groups has yielded detailed information on variety of physical properties of the ICM/IGM, such as on gas ionization balance, temperature structure, chemical composition, and more [e.g., Pinto et al., 2015, Ahoranta et al., 2016, de Plaa et al., 2017, Mernier et al., 2018]. Such information can be used to tackle some of the open questions of the evolution
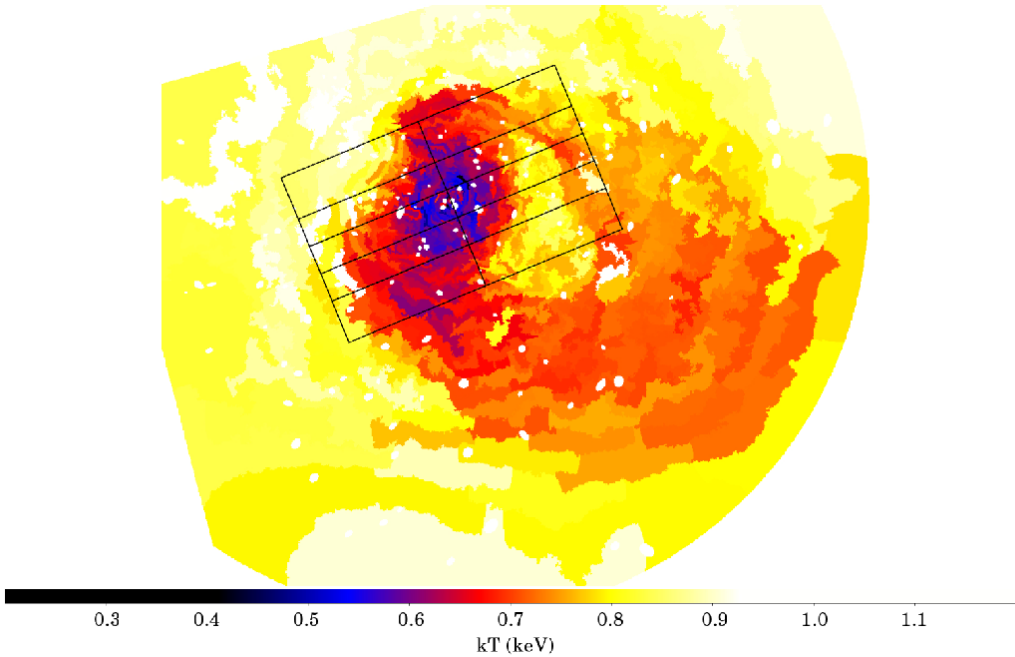
Figure 1.3: Temperature map of IGM at the core region of galaxy group NGC 4636. The gas has been distorted by previous AGN outbursts and possible core sloshing motions. The overlayed rectangular regions mark various spectral extraction regions used in analyzing the emission in moderate and high energy resolution regimes. The figure is adopted from Paper IV.

of the cosmic structures, such as the heating mechanisms of ICM/IGM (a so–called cooling flow problem), or metal enrichment of inter–galactic gas, for instance. In this context, high energy resolution X–ray spectroscopy holds a great promise, as it unlocks observational possibilities that are not accessible with moderate energy– resolution instruments (as demonstrated, e.g., in Papers IV and V). However, as is later discussed in this thesis (Chapter 3), the current X–ray instrumentation can- not fully redeem the promise of high energy resolution spectroscopy, because these spectrometers were designed to study point sources instead of extended ones. Nev- ertheless, in Papers IV (see Fig. 1.3) and V we tried to push the limits of these spectrometers to reveal glimpses of the realm that will ultimately be opened up by the next generation of X–ray observatories (discussed in Chapter 4).

2 Tracing the thermal and Hydrodynamical Properties of Diffuse Plasma

The present high energy resolution X–ray instruments provide a possibility to measure and resolve some of the most important X–ray lines that are emitted in the physical conditions occurring in the intra–cluster/group media. As the line emission transmits direct information on the inner atomic states of the emitting atoms, careful spectroscopic analysis of the emission line spectra provides a variety of information on the physical conditions present in the emitting gas. Information on properties such as ionization balance, temperature, chemical composition and others may be obtained from direct measurements of intensities of spectral lines produced by different high–Z ions, and by examining the relative intensities between them.

High energy resolution X–ray absorption spectroscopy, on the other hand, expands the observational possibilities to less denser and/or dilute gas environments whose X–ray emission is too weak to be detected. Considering the large–scale structure of the Universe, such environments are found, e.g., at the hot galactic halos, outer parts of IGM/ICM, or in the WHIM residing in the filamentary structures of the cosmic web. While similar physical information can be obtained through both emission and absorption line spectroscopy, an obvious limitation regarding to the absorption line studies is that they are limited only to those objects that happen to intervene a line–of–sight towards a bright, X–ray continuum source.

2.1   Line Emission of Thermal Plasma

The line emission refers to signals of ionic electrons' radiative transitions from excited states back towards their ground states. While X-ray line emission can result from variety of different kind of excitation/ionization processes, in thermal plasma, the excitations are typically due to collisions between the free electrons of the plasma with ions (i.e., by giving energy to the bound electrons). This is particularly the case

in collisionally ionized diffuse plasma, which is expected to be the dominant state in ICM/IGM. In WHIM, collisional ionization equilibrium is expected to become important in environments where ionic number densities and gas temperature are sufficiently high (e.g., see Fig. 11 in Wijers et al. 2019), although the collisional excitation driven line emission signal from WHIM is too weak to be detectable in individual objects with use of current high energy resolution X–ray spectrometers.

Since the possible energy states of electron excitations are quantized and ion depend, the line emission spectra of different ion species each have their unique spectral 'fingerprints' with fixed transition line energies that readily enables one to identify the line emitting ions from high resolution spectra when the source redshift is known. The case is more complex when considering the line emissivities of various collisionally driven ionic lines arising from diffuse CIE (collisional ionization equilibrium) gas, as the line powers are transition specific and somewhat environment sensitive. Generally however, the line emissivities from diffuse, thermal plasma may be calculated using a relation that is of a form [Osterbrock, 1974]:

$$\int \epsilon_\nu^{line} d\nu \propto n_i\, n_e\, \frac{h\nu \Omega(T)\, B}{\omega_{gs}(n_i)} \left(\frac{1}{kT}\right)^{1/2} e^{-E/kT}. \qquad (2.1)$$

Here, n_i and n_e are the ion and electron number densities, $h\nu$ the energy of the transition, $\Omega(T)$ a 'collisional strength' -function (needs to be derived empirically), B the branching ratio for radiative decay through the transition, ω_{gs} is the statistical weight of the excited energy level, and E the excitation energy relative to the ground state. The equation indicates that the line emissivity of a given transition scales linearly proportional to the product of ion and electron density and otherwise depends only on temperature. The collisional strength function varies typically only slowly as a function of temperature, thus meaning that the ratios between the strengths of different emission lines of the same ion change only moderately at the temperature ranges that are observationally meaningful (see the example in Fig. 2.1).

In realistic case of emission line spectrum analysis of astrophysical sources, one has to consider all ionic spectra of different elements simultaneously, which is an exercise also requiring the information on relative abundances of the elements. In practice, one does not have to iterate through the whole parameter space of different ion species by hand in order to find the best match for a given spectrum using Eq. 2.1, but there are sophisticated and well–tested spectral fitting tools designed to perform exactly this task. These models are usually fitted to the data by varying just a few of the key parameters of interest (e.g., T and n_H). Indeed, in the papers including spectral analysis of IGM emission line spectra (Papers IV-V), we have used the MEKA [Mewe et al., 1985, 1986] –based, collisional ionization equilibrium modelling
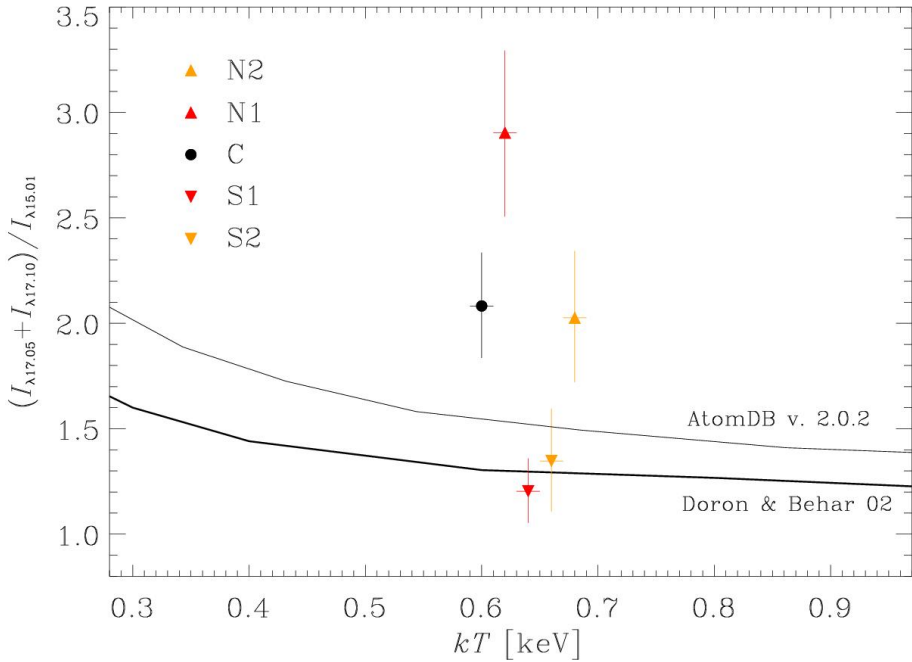
Figure 2.1: Temperature dependency of optically thin line intensity ratio between resonant ($\lambda_0 = 15.01$ Å) line and a doublet at $\lambda_0 \approx 17.1$ Å. The two models are shown with the black lines: AtomDB v. 2.0.2 [Loch et al., 2006] and Doron and Behar [2002]. The figure was adopted from Paper IV.

tool, ran with SPEX [Kaastra et al., 1996, Kaastra et al., 2018] spectral analysis software (i.e., the SPEX 'CIE'-model). We only deviated from this approach when no appropriate theoretical solution was found, which readily indicates the presence of additional physical processes (or unresolvable gas phases) within the examined source. For instance, the ionic emission spectra models do not account for possible line–of–sight absorption of the emitting medium itself, which can skew the measured line ratios in case the strongest (resonance) lines are optically thick. We discuss this process and the additional information that such self-absorption can provide on in more detail in Paper IV.

It is worth noticing that in line emission of thermal plasma, the radiative decay of excited electrons essentially converts plasma's kinetic energy into photons, which leads to gradual cooling of the gas. As emissivity is proportional to the product of ion

and electron density, such radiative cooling is more efficient in denser environments. Without the existence of counterbalancing heating mechanism, it would therefore be expected that in denser parts of diffuse CIE gas (that can be assumed to be initially close to isothermal state), such as in galaxy cluster and groups, the denser core regions cool faster than the outer parts. Since cooling decreases the thermal pressure, the cooled, denser gas should sink towards the center of the gravity. The signal of such process is imprinted in X-ray emission line spectra, as the line emission is the mechanism removing the heat out of the system. Following this line of thought, one would expect the cooling flows to lead to enhanced star formation rates in the central galaxies of cool core systems, a prediction that has not been supported by observational data of such systems. It is currently expected that the explanation for this is that the cooling flows trigger AGN outbursts, thereby leading to re–heating of the cool gas at the core regions through effects of shock–heating and turbulent mixing. Again, the signal of the heating process will be largely imprinted on X-ray emission spectra. We study the cooling flows of cool core systems in Papers IV and V.

2.2   Absorption in Thermal Plasma

Since the power of emission lines depends on the volume density of the respective ions (Sect. 2.1), the instrumental sensitivity and calibration accuracy place a limit for n_i below which the emission signals can no longer be detected. In practice this means that with current X-ray instrumentation, the line emission generated in individual low ion–density structures, such as hot galactic halos, outskirts of ICM/IGM, or filamentary WHIM, cannot be studied through emission line analysis. In such cases, one can rely on absorption line studies, as the line absorption strength depends only on the total ionic column density, $N_i = \int n_i dl$, through the absorbing medium.

The line absorption signal is formed when a fraction of the background source emitted photons interact with the ions of an intervening gas structure through a process of photoexcitation. In photoexcitation, the photons whose energy matches the energy difference between two discrete atomic energy levels (in absorbing ion's rest frame) can excite electrons from lower energy states to higher ones, while the probabilities for such absorption processes are transition dependent. The photo–excited electrons will return quickly back to their ground state (with typical timescale $\sim 10^{-8}$ s) by emitting photons with energies corresponding to the taken downward transitions. Since these photons are emitted to random directions, an observer measuring the background source photon flux from a single viewing angle will detect dips

in a photon flux at the energies of the transitions.

As might be intuitively expected, the fraction of absorbed photons is proportional to the product of the integrated number of ions through the sight–line, N_i, and the probability that a given photo–excitation will take place (commonly quantified in terms of the oscillator strength of the transition, f). It is convenient to quantify the spectral absorption lines in terms of their equivalent widths (EW), which is a directly measurable spectral quantity. It can be shown that in optically thin regime, the equivalent width of a spectral absorption line at wavelength λ ($\lambda = hc/E_{ph}$) equals to

$$\mathrm{EW}_\lambda = \frac{N_{i,1}\, f_{1,2}\, e^2\, \lambda^2}{4\epsilon_0\, mc^2}. \tag{2.2}$$

Here, $N_{i,1}$ is the column density of ion i in some lower energy state 1, $f_{1,2}$ the oscillator strength of transition between energy levels 1 and 2, e electron charge, ϵ_0 vacuum permittivity and m electron rest mass. In observer's perspective, it is often usefull to define EW as integrated line flux over a spectral feature:

$$\mathrm{EW}_\lambda = \int \left[1 - F_\lambda/F_0\right] d\lambda, \tag{2.3}$$

where F_λ refers to flux at wavelength λ and F_0 to continuum level without absorption. It is worth noticing, that even if Eq. 2.3 is defined in terms of F_0, EW is fully independent of it.

In practice, cosmic X–ray absorbers consist of large number of different ion species and potentially complex thermal/velocity–field structures. The absorption fingerprints can therefore be intrisically very complex, a fact that is worth to bear in mind when studying and interpreting the signals in noise limited spectral data.

2.3 Measuring the properties of Diffuse Plasma

The emission and absorption line analysis of high energy resolution X-ray spectra yields several types of information that is not typically obtainable with the use of moderate energy resolution instrumentation, such as conventional CCD arrays detectors. Below I provide a brief summary of some of the high–resolution specific analysis methods that were applied in the papers of this thesis.

EMISSION:

1) CIE line emission modeling (Sect. 2.1) provides T –constraints on X–ray emitting gas. The constraints can be utilized in examining the thermal properties of X–ray emitting, diffuse gas structures, such as ICM/IGM. In addition, multiphase CIE modeling can be used to study the thermal structures of the X–ray emitting gas, and to estimate the magnitude of cooling flows in cool core clusters/groups (applied in Papers IV and V).

2) Resonant line scattering can be used to measure the level of self–absorption at X–ray emitting gas structures. When information on n_i and N_i is available, the level of resonant scattering yields constraints on the line–of–sight velocity distribution for the ions (Paper IV).

3) Extracting and analyzing diffraction spectrometers' data at different cross–dispersion angles can yield information on the radial profiles of various physical parameters of interest. This method is only applicable for bright, extended sources, such as nearby galaxy groups and clusters (Paper IV).

ABSORPTION:

4) Relative strengths of lines that are produced by different ion species of the same element provide a useful tool to measure the temperature of absorbing gas (e.g., EW(O VIII Lyα) vs. EW(O VII Heα)). Notably, even upper limits of an undetected line can yield a useful T constraints towards one end, in case an ionic line of lower/higher ionization state is well detected (see Papers I and II).

5) Ion column density constraints at metal–rich absorbers can be used to place limits on absorber metallicity, $Z_{abs.}$, by comparing them to the measurement limits on co–locating FUV HI Lyα absorption. In addition, comparison of X–ray band measured ion column densities to the ones measured in FUV band can yield information on thermal structure of absorbers (Papers I and II).

In addition to the above, in the next sub–section I discuss a method that allows one to place limits on a line–of–sight velocity distribution of an absorber with minimal observational requirements.

2.3.1 WHIM Absorption and line–of–sight velocity dispersion

One shortcoming of present high spectral-resolution X-ray instruments is that their resolving power is insufficient to measure the widths of the narrow ($b <$ few hundreds of $\mathrm{km\,s^{-1}}$) X-ray lines directly. A spectral line profile is a convolution between the intrinsic shape of the observed line and the instrumental line broadening function, the latter of which arises from the physical realization of the measurement device. In typical astrophysical context, this means that the widths of (stand–alone) spectral lines express mainly the characteristics of the measurement instrument itself.

To overcome this limitation, one could try, in principle, to deconvolve the instrumental line broadening using the calibration data on the instrument performance so as to obtain the true line shapes, but unfortunately this approach is very sensitive to several sources of uncertainties and is therefore not useful. As a work around for the instrumental limitations we have therefore introduced a method that enables determination of the broadening of absorption lines by relying on the measurements of line equivalent widths, EW_λ, which is an invariant parameter in the instrumental line broadening process. In what follows we focus only on the two strongest absorption lines produced by the O VII ion, but in principle the method could be applied to any other ion species whose line fluxes are sufficiently high to exceed the detection threshold of current high energy resolution X–ray instruments.

We take use of the fact that the strongest O VII absorption line, O VII Heα ($\lambda_0 = 21.602$ Å), begins to saturate at the line center at $\log_{10} N_{\mathrm{OVII}}(\mathrm{cm^{-2}}) \sim 15$ level, i.e., roughly at the same column density which enables X-ray detection of this line ($\log_{10} N_{\mathrm{OVII}}(\mathrm{cm^{-2}}) = 15 \rightarrow \mathrm{EW}_\lambda$ (O VII Heα) ≈ 3 mÅ). In contrast, the second strongest line produced by the same ion, O VII Heβ ($\lambda_0 = 18.628$ Å), will remain optically thin up to almost ten times higher O VII ion column densities. In addition, the optical depth at a line center depends also on the line–of–sight velocity dispersion of the absorbing ions. I demonstrate that in Fig. 2.2, where I plot the curve of growth for O VII Heα and Heβ lines for two different values of the Doppler spread parameter, b. It can be seen that the value of b has a strong effect on the relative fluxes of O VII Heα, Heβ lines within the detectable WHIM N_{OVII} range.

The $\mathrm{EW}_{\mathrm{He}\alpha}/\mathrm{EW}_{\mathrm{He}\beta}$ thus provides a sensitive diagnostic tool for O VII absorber ion velocity distribution along the line–of–sight, and notably, it works most effectively in the b –range that is far below the accessibility of direct line width measurements. In particular, I note that the upper limit on $\mathrm{EW}_{\mathrm{He}\beta}$ constrains the lower limit on b, so that useful information on the velocity dispersion can be obtained always when O VII Heα line is well–detected. This is demonstrated in Fig. 2.3, where the behaviour of $\mathrm{EW}_{\mathrm{He}\alpha}/\mathrm{EW}_{\mathrm{He}\beta}$ –ratio is examined as a function of the b –parameter at several fixed,
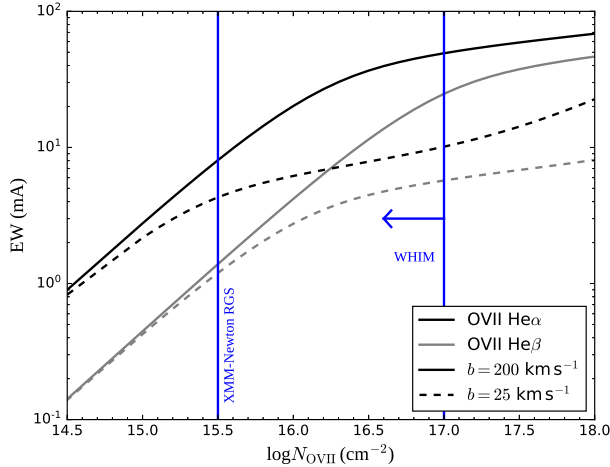
Figure 2.2: O VII Heα and Heβ line equivalent widths as a function of O VII column density for velocity dispersion $b = 200$ km s^{-1} (solid lines) and $b = 25$ km s^{-1} (dashed lines). The blue line on the left hand side shows nominal RGS (1st spectral order) detection threshold for N_{OVII}, while the blue line on the right marks a rough maximum for O VII column density expected at WHIM absorbers.

X–ray detectable O VII column densities.

On the other hand, the Doppler spread parameter is described by:

$$b_i = \left[\frac{2kT_i}{m_i} + b_{non-th.}^2 \right]^{0.5}, \qquad (2.4)$$

where k is the Boltzmann constant, T_i the ion temperature, m_i the mass of the ion, and $v_{\text{non}-\text{th.}}$ the non-thermal velocity dispersion of the absorbing gas. Eq. 2.4 indicates how a measurement of the linewidth can give important insights on the physical conditions of the absorbing gas, such as an upper limit on the ion temperature, for instance. If the ion temperature limits have been obtained by other means (e.g., from measurement of ion fractions), then the equation can be used in constraining the non-thermal broadening component. We demonstrate the capability of this method with a practical application in Paper I.
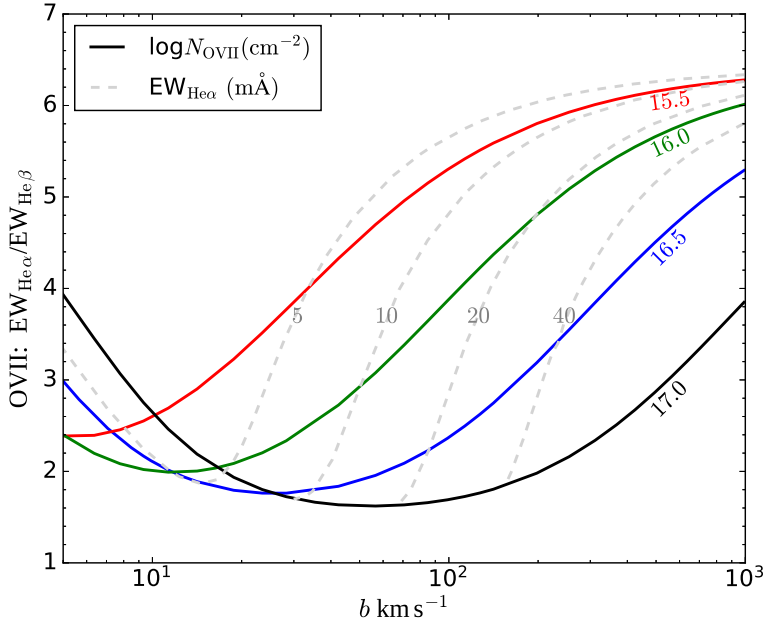
Figure 2.3: Heα and Heβ line equivalent width –ratio plotted as a function of b. The solid curves are for constant $\log_{10} N_{OVII}(cm^{-2}) = 15.5 - 17.0$, and dashed curves for constant $EW_{He\alpha} = 5 - 40$ mÅ. Here, the various crossing points between dashed and solid curves correspond to valid solutions between $EW_{He\alpha}$, $EW_{He\alpha}/EW_{He\beta}$, N_{OVII} and b_{OVII}. The figure was adopted from Paper I.

3 High Energy Resolution Spectroscopy Instrumentation

As it stands, the most powerful spectroscopic instruments in X–ray astronomy utilize photo–dispersion–effect–based measuring techniques. Grating spectrometers provide outstanding capability to detect and resolve individual spectral lines, as their performance is not constrained by fundametal limitations, such as the Fano noise [Fano, 1947], which limits the resolving power of charge-coupled devices (CCDs). The two most important high energy resolution instruments focused on the soft X–ray band are the XMM–Newton Reflection Grating Spectrometer (RGS) and the Chandra Low Energy Transmission Grating (LETG) spectrometer. These instruments are introduced briefly in the following sections. The next generation space–borne X–ray instrumentation capable in spatially resolved high energy resolution spectroscopy are currently under development, are discussed briefly in Chapter 4.

3.1   XMM–Newton RGS

The XMM–Newton X–ray observatory provides the largest effective area in the soft X–ray band. The satellite comprises of three parallel X–ray telescopes, two of which are equipped with identical high resolution instruments; the Reflection Grating Spectrometers #1 and #2 (hereafter RGS1 and RGS2). The RGS instruments' cover spectroscopic range between 5–35 Å (2.5–0.35 keV) with blaze wavelength at 15 Å, achieving $A_e \approx 50 - 60$ cm^2 per instrument around $15 - 20$ Å (Fig. 3.1). This band covers the rest wavelengths of number of plasma-diagnostically interesting X–ray lines, including Fe and O, K and L shell transitions, for instance.

The RGS grating assemblies, consisting of ≈ 200 diffraction gratings per instrument, are mounted in the back of Wolter I type X–ray optics. During exposures, about a half of the incoming photons interact with the gratings and deflect to a small off–set angle that is described by the dispersion equation:
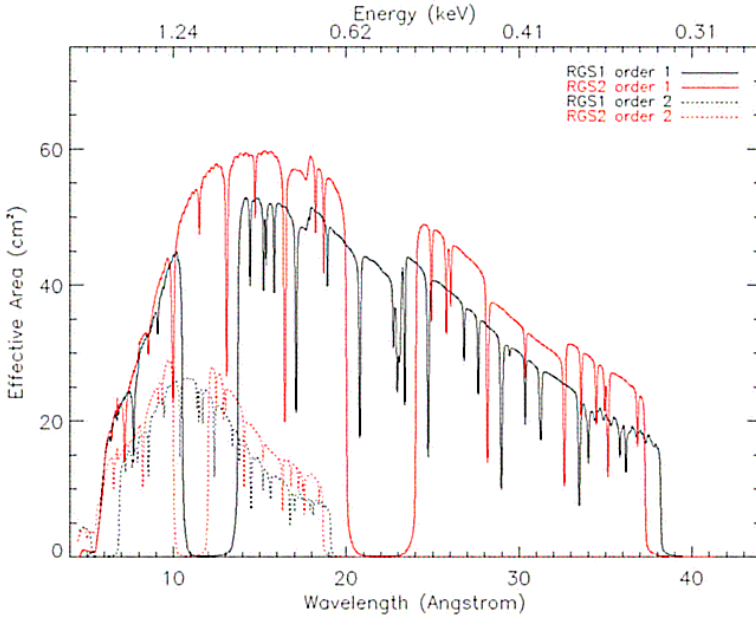
Figure 3.1: Effective areas of RGS1 and RGS2. The different curves show the A_e of different instrument/spectral order as indicated. The two wide dips in first spectral order effective area, seen just above 10 Å in RGS1 and above 20 Å in RGS2, are due to failed CCD chips. The numerous narrower dips are due to detector gaps and CCD pixels with abnormal response. Credit: ESA

$$m\lambda = d\left[\cos(\beta) - \cos(\alpha)\right]. \tag{3.1}$$

Here, m denotes the spectral order, λ is the wavelength of the incoming photon, d the charasteristic groove spacing ($\approx 600\,\mathrm{mm}^{-1}$ in RGS), and α and β are the incident and diffraction angles of the photon, respectively. The refracted photons are recorded with the RGS cameras, which consists of 9 adjacent, 1024×384 pixel CCD arrays that are implemented to follow the curvature of the Rowland circle. To supress the aberration effects due to converging X–ray radiation, each individual grating element has been fine–tuned to project the $\lambda = 5 - 40$ Å, $m < 0$ dispersion spectrum to the exact same physical location. When the telescope is aimed directly towards the source of radiation, the refracted photons form a linear dispersion spectrum that runs along the CCD array cross–dispersion center axis at the RGS detector plane.

The RGS instruments record detection times, pixel coordinates, and energies (or more accurately, the electric charges produced within CCD pixels) of each photon that gets absorbed in the detectors. The event time information can be used to perform photometric measurements, or as an input in generating the good time interval (GTI) files (in practice by examining the event rate at RGS CCD array #9s, whose signal is dominated by energetic particles rather than source photons). As different spectral orders are overlapped in the projected dispersion spectrum, the intrinsic energy resolution of the CCD pixels are used to separate the overlapping spectral orders. The energy resolution of the dispersion spectrum itself is defined by the line–spread function that is an end result from various physical charasteristics of the telescope (and also m). In the first spectral order, the RGS instruments provide energy resolution $E/\Delta E = 100 - 500$ and achieves ≈ 5 Å wavelength accuracy.
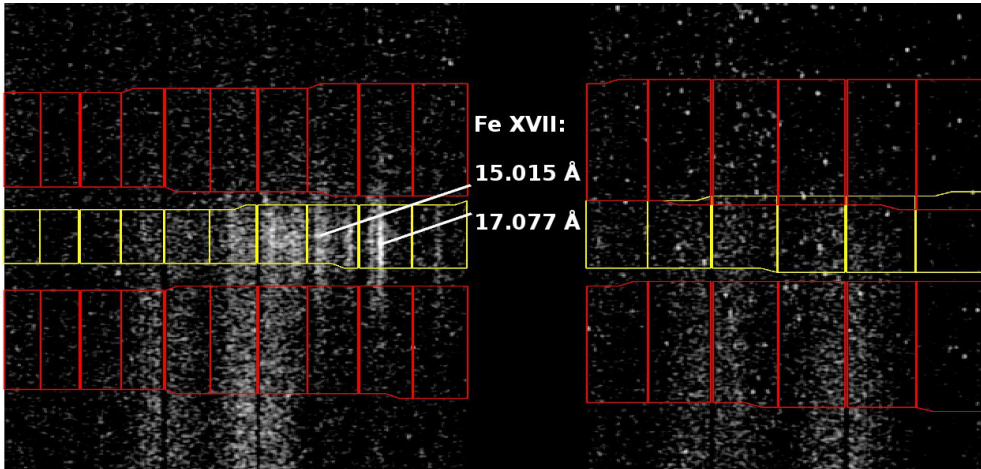
Figure 3.2: Spatial image of RGS2 exposure on galaxy group NGC 1404 demonstrating the principle how 1D spatial information can be obtained from RGS data. The yellow contours enclose a spectral exraction region at the peak of the X–ray flux. The red contours show two additional spectral regions extracted $\sim$ symmetrically from both sides of the peak. The white arrows point to signals of two intense emission lines, produced by the Fe XVII ions that are abundant in the IGM of this group.

The RGS spectrographs are slitless and not capable of imaging observations. Nevertheless, 1D–spatial information is available in the cross–dispersion direction, which covers about 4.8 arcmin angle in the sky. It is therefore possible to attain

partial spatial information on extended objects by extracting spectra from different cross–dispersion angles of the same observation (see Fig. 3.2). In practice, however, extracting spectroscopic information from extended sources requires that the 2D–flux distribution of the source emission is known so that its effects on spectrum can be corrected for. Without appropriate correction in place, the spectral energy resolution will degrade, as the spectral wavelength solution assumes that all the photons come from the same exact (dispersion) direction. In practice such correction can be performed with use of additional, imaging X–ray data measured from the same source at the same energy band. Such complementary data can be obtained, e.g., from moderate energy resolution instruments at XMM–Newton main focal plane that run simultaneously with the RGSs. In Paper II, we demonstrated the uselfulness of such a measurement approach by acquiring some novel type of observational information that can be extracted from RGS data of extended sources.

3.1.1   On the co–addition of RGS spectra

The XMM–Newton raw data is most commonly processed with the XMM–Newton Science Analysis System (SAS) `rgsproc` data reduction pipeline[1], as was also done throughout the papers included in this thesis. The pipeline allows a user to fine–tune the calibration according to ones specific requirements, and we have learnt that such fine–tuning is beneficial in absorption analysis at weak–line regime. Namely, we remove the cool pixels (i.e., the pixels with abnormally low reponse) from the data, correct for pixel–dependent energy offsets (`rgsproc rgsenergy` option with-diagoffset=yes), increase the accuracy of aspect drift correction by a factor of two (driftbinsize=0.5″) and calculate the grating line spread function using the full available convolution space. In case we prepare the spectral data for stacking purposes, we also utilize the `rgsproc` binning tool to re–bin the spectral data into 20 mÅ spectral bins.

In general, the `rgsproc` generated, observation specific spectra, response matrices and backgound files can be co–added with the use of a SAS tool `rgscombine`, so as to simplify the analysis of large observation samples. However, the `rgscombine` tool assumes the source flux to be constant accross all the co–added observations, which is not (typically) the case for AGNs. Indeed, the more the source flux varies between co–added observations, the more calibration issues are expected to arise in the final, co–added spectrum [as described, e.g., in Kaastra et al., 2011]. Therefore, it is wise to analyze individual spectra simultaneously whenever possible, rather than analyze a co–added spectrum. However, if a large number of observations needs to be analyzed

---

[1]http://xmm-tools.cosmos.esa.int/external/sas/current/doc/rgsproc/node3.html

simultaneously, then the only practically viable option is to rely on analyzing the co–added data.

In Fig. 3.3 I plot the co–added RGS1 1st order data of the three longest exposures[2] made on quasar 3C 273, modeled with a simple powerlaw model over a $17 - 23$ Å spectral band. The data were reduced twice for this figure, using two different sets of `rgsproc` processing parameters: 1) The default `rgsproc` processing with cool pixels (that are prone to cause false spectral features) removed, and 2) More accurately conducted `rgsproc` data processing, as described in the first paragraph of this section. In what follows, the data from the former processing options is called as "default reduction", and the latter one as "detailed reduction".

Examining Fig. 3.3, it can be seen that co–adding the spectral data produced with `rgsproc` default processing options fails to model the various instrumental features appropriately. In fact, inspecting the fit residuals at the location of RGS1 instrumental features (as indicated by the various dips in the response–convolved continuum model on the "detailed reduction" spectrum) reveals that adoption of this approach can lead in to false, absorption–direction oriented spectral artefacts at the locations of abnormal instrument responses. Given the relative large number of such defects in XMM–Newton RGS instruments, these calibration issues can become notably problematic in studies of weak absorption signals in co–added RGS data. I visualize these problems in the figure by the marking the rest–wavelengths of two diagnostically important oxygen lines (O VIII Lyα and O VII Heβ); It can be seen that both of these wavelengths coincide with badly modeled calibrated specral bins, and thus any measurements made on these features would lead to biased outcome.

The situation is improved when using the detailed reduction approach. As indicated in Fig. 3.3, this processing leads to lower scatter of the data points (especially absorption–like features at the location of rapidly changing response bands) and to improved fit statistics (in this case, about 15 %). However, one needs to be cautious when applying non–standard processing options (for the case they have not been tested thoroughly by the developers) and always check their effect on the overall quality of the spectrum afterwards.

3.2   Chandra LETG

The measuring instruments onboard the Chandra X–ray observatory provide the best spatial resolving power for imaging observations and the best energy resolving power for spectroscopic measurements in the X–ray band. The satellite carries two

---

[2]Obs. ID's 0136550101, 0414190101 and 0414191401

high energy resolution instruments: the Low Energy Transmission Grating (LETG) spectrometer that is optimized to measure lower photon energies ($0.070 - 10$ keV, corresponding $1.2 - 175$ Å) and the High Energy Transmission Grating (HETG) for higher energies. The energy bands of the two instruments' overlap partially in soft X–ray, but since LETG provides significantly larger effective area at the band of interest in this work ($\lambda \approx 10 - 40$ Å), only the LETG is discussed here.

The LETG is a moveable grating assembly that can be employed at will below the Chandra's Volter I type X–ray mirrors, the High Resolution Mirror Assembly (HRMA). When in place, the LETG assembly intercepts the full X–ray flux that exits the HRMA. The grating assembly consist of 580 grating elements installed on ring–shaped structures that are mounted on an aluminium support structure. Each grating element comprises thin parrallel gold threads with string density $p \approx 1000$ mm^{-1}. The intercepted photons will refract by angle θ following the diffraction equation, $m\lambda = p \sin(\theta)$, and form a disperse spectrum to Chandra's main focal plane. There, the spectrum can be recorded with two alternative instruments; The High Resolution Camera (HRC), or the Advanced CCD Imaging Spectrometer (ACIS).

The HRC consist of two micro–channel plate imaging detectors, the HRC-I and HRC-S. HRC-S is a the default detector for capturing the LETG dispersion spectra and consist of three segments tilted to follow the curvature of the LETG Rowland circle. The ACIS detector assembly includes 6 adjacent CCD arrays (i.e., ACIS-S) that are designed for HETG observations, but can be used to record LETG spectra as well. During the LETG observations, both positive and negative spectral orders are recordered and can be later combined to improve the spectral S/N, and to fill the detector gaps in the data (see Fig. 3.4).

The choise of the detection instrument depends ultimately on the specific observational needs. The micro–channel plate detection techique enables detection of lower energy photons, and indeed, the LETG+HRC-S combination covers a band of $1.2 - 175$ Å with an outstanding energy resolution $E/\Delta E > 1000$ at $50 - 160$ Å and $E/\Delta E \approx 20 \times \lambda$ below. The LETG+ACIS-S wavelength band is limited to $1.2 - 60$ Å, where it yields a similar energy resolution than the HRC-S. The LETG+HRC-S combination also provides larger A_e from $\lambda \approx 15$ Å upwards (see Fig. 3.4). However, poor intrinsic energy resolution of the HRC-S detector excludes the possibility to separate the different spectral orders of the same prefix, which can hamper the physical interpretation of complex line spectra.

The LETG instruments provide a nominal wavelenght accuracy of 5 Å. However, in–flight evidence has shown that the LETG+HRC-S dispersion relation has several non–characterized non–linearities, some of which have been cured with a help of Chandra in–flight data on celestial calibration sources [e.g., Chung et al., 2004].

Nevertheless, origins of some non–linearities remain unclear, which makes their spectral effects difficult or impossible to predict in a reliable way. It is unclear whether LETG+ACIS-S combination suffers from similar characterization problems. As dispersion spectrum location at the detector plane shifts from exposure to exposure, being dependent on the telescope aimpoint relative to that of the observed source, the non–linearities can prove problematic in various type of analysis. This underlines the crucial role of extensive ground calibrations when it comes to space–borne instrumentation.
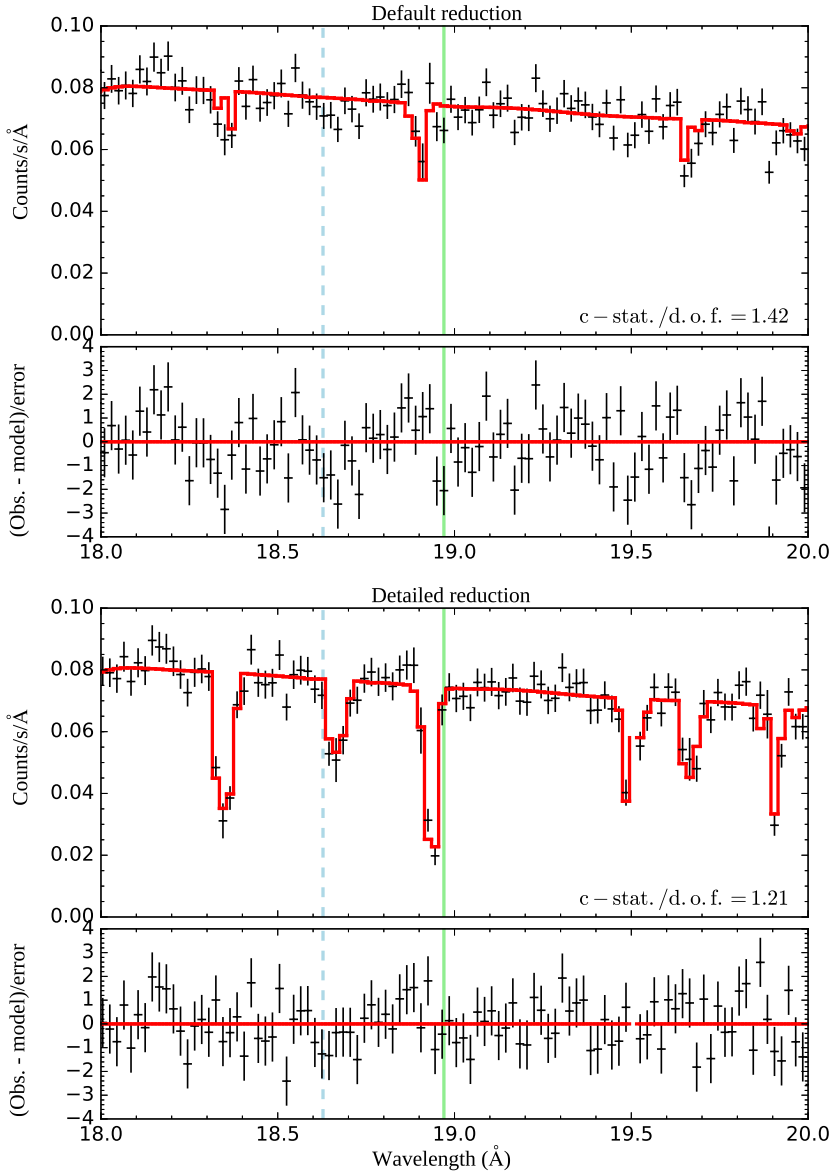
Figure 3.3: Best–fit continuum model (red curves) to a co–added spectrum of three longest exposures on quasar 3C 273. Upper panels: The spectrum and fit residuals of a powerlaw model minimized to a data reduced with default `rgsproc` parameters. Bottom panels: The same as above but the data was reduced with somewhat more accurate processing options (see text for details). The two vertical lines indicate the rest–wavelengths of O VIII Lyα (green colour) and O VII Heβ (blue dashed line). The reduced Cash–statistic values over $17 - 23$ Å wavelength band are indicated.
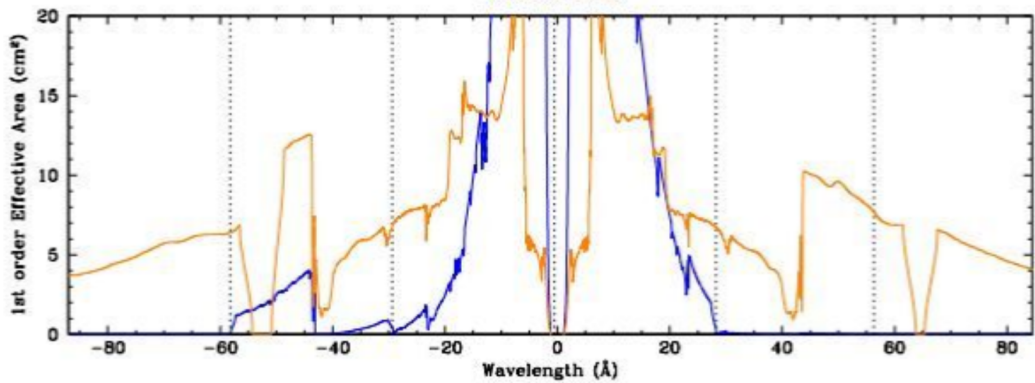
Figure 3.4:   Fist order effective areas of LETG+HRC-S (orange line) and
LETG+ACIS-S (blue line) combinations as measured in laboratory before launch.
The dashed lines mark the chip boundaries in ACIS-S. Using a small offset in tele-
scope pointing shifts the plus and minus order dispersion at the detector plane, thus
enabling that all the wavelengths can be sampled. The figure covers a band includ-
ing the rest wavelengths of most important spectral lines that are produced by hot,
$\sim 10^6 - 10^7$ K gas. The figure was adopted from the Chandra Proposers' Observatory
Guide.

4 The future: Observational prospects of Athena X-IFU

Advanced Telescope for High Energy Astrophysics (ATHENA) X–ray observatory is an L2 mission in ESA's 'Cosmic vision' -program, scheduled to be launched in the early 2030's. ATHENA's main instrument, the X–ray Integral Field Unit (X-IFU), is an array of cryogenic micro–calorimeter detectors fine–tuned to measure photons at energy range $0.2 - 12$ keV ($1 - 60$ Å) with a targeted 2.5 eV FWHM energy resolution level below 7 keV [Barret et al., 2016] and $\lesssim 3.0$ eV above. The current detector array concept (as of fall 2022) consist of 3840, $5''$ sized Transition Edge Sensors (TES) in a hexagonal arrangement that provides $\approx 5'$ angular diameter field of view in the sky. However, the final design of the X–IFU is still to be revised due to budget overrun issues and it is therefore possible that the above mentioned figures will be somewhat downgraded. Regardless of the possible design adjustements, the X–IFU will deliver breakthroughs in X–ray observational capabilities, owing largely to the TES –based photon detection technique the instrument utilizes. This technology is novel in astronomical instrumentation setting and the only available one that enables the construction of large detector arrays with high energy–resolving power pixels. The applicability of cryogenic X–ray micro–calorimeters' in space–born observations has already been successfully demonstrated by the (unfortunately short–lived) Japanese Hitomi mission [Takahashi et al., 2014], whose successor, XRISM [XRISM Science Team, 2020], is scheduled to be launched in spring 2023.

The science with Athena X–IFU is expected to produce significant advances in the field of observational X–ray astronomy due to number of upgrades as compared to the current high–resolution instruments. These include, for instance, up to two orders of magnitude increase in effective area over the XMM-Newton RGS energy–band (see Fig. 4.1) and the capability in spatially–resolved high energy resolution spectroscopy. The increased effective area translates into improved sensitivity, while the imaging capability opens possibilities to examine extended X–ray sources in unpresented detail. X–IFU's broad energy band, on the other hand, enables simultaneous

recording of spectral features produced in variety of different type of physical environments. In addition, the telescope itself has been planned to have the ability to do swift re–pointings, so as to catch Gamma Ray Burst (GRB) afterglows whenever such events take place. However, this capability is currenlty under a threat do to the Athena re–design process.

In Fig. 4 the outstanding performance of X–IFU is demonstrated with a comparison to that of XMM–Newton RGS1 instrument[1]. In the figure, the two panels show simulated data corresponding 100 ks exposures on a common source with each instrument. The data was simulated using a time–averaged X–ray data on quasar 3C 273 as a base–model. The figure shows a zoom–in around the rest–wavelength of O VII Heα absorption line, i.e., the strongest absorption line produced by the hot Galactic halo. The line signal models absorption through $\log_{10} N_{\mathrm{OVII}}(\mathrm{cm}^{-2}) = 16$ ion column, (corresponding $\mathrm{EW}_\lambda \approx 18$ mA or $\mathrm{EW}_{h\nu} \approx 0.5$ eV) in this example. The X–IFU is able to resolve the line with a great accuracy, whereas in RGS data, the signal is only marginally detectable.

As discussed in detail, e.g., in Barret et al. [2016], the main scientific objectives of X–IFU are to:

- Study the evolution, distribution, properties and dynamics of hot plasma in the cosmic web

- Track the evolution of super–massive blackholes/AGN and study the feedback processes between them and the host galaxies/the intergalactic medium

- Utilize instrument's unique measurement capabilities to contribute to the observational astrophysics of the 2030's

In the context of the science questions relevant to this thesis (mainly the first item above), it is worth noting that the observational prospects of X–IFU offers more than just an improved sensitivity enabling detections of increasingly weaker absorption/emission signals. In fact, the spatial resolving ability plays an important role both in ICM/IGM and WHIM studies. For instance, one requires both high sensitivity and the spatial information of the detected photons in order to study the line emission from the outer parts of ICM/IGM. Such measurements are partially possible with the use of current dispersion spectrometers (Sect. 3.1 and 3.2), but as noted ealier, require complementary, prior knowledge of the 2D spatial distribution of different X–ray emitting gas phases to avoid spectral line smearing.When it comes to

---

[1]Note that similar difference would be expected between X–IFU and XRISM as well, as indicated by Fig. 4.1

measuring the weak emission lines from filamentary WHIM, overcoming such spectral line smearing is crucial.

The X–IFU is expected to detect a statistically meaningfull sample of WHIM absorbers from a redshift 0 to a few. Along with other observations, such as the complementary X–ray observations from outskirts of ICM and measurements in other wavelength bands, the evolution of the missing baryons will be likely understood in a comprehensive way. For example, Kaastra et al. [2013] studied Athena X–IFU's prospects to detect hot WHIM absorbers. The authors considered an observation scheme where 25 AGN and 40 GRB afterglows are observed during the Athena mission, totaling 7 Ms worth of exposure time altogether. They found that given the X–IFU figure of merit, such an observation program should lead into detection of $\approx$ 200 WHIM X–ray absorbers, of which $\approx 1/3$ would be analyzable in emission regime, as well. Considering the information carried by emission and absorption together yields more physical information on the source than either of them separately.

Finally, I note that the numbers of X–IFU detectable WHIM absorbers also depends on the re–design of the Athena. However, the WHIM absorption studies belong to observationally less ambitious science cases officially planned for the X–IFU, and should therefore not be severely affected by the possible changes in the Athena X–IFU key parameters. In fact, if the re–design of Athena would lower X–IFU's technical performance to a level insufficient for WHIM observations, then that would mean almost all the proposed X–IFU science would be infeasible, too. However, in case of WHIM we need to consider another unknown as well, i.e., the correctness of the theoretical predictions for the observable WHIM properties. It is therefore worthwhile to conduct the hot WHIM phase studies already with current instrumentation, and with the XRISM, when operative. With this work we can try to ensure that the X–IFU will be optimized to fulfill its mission goals.
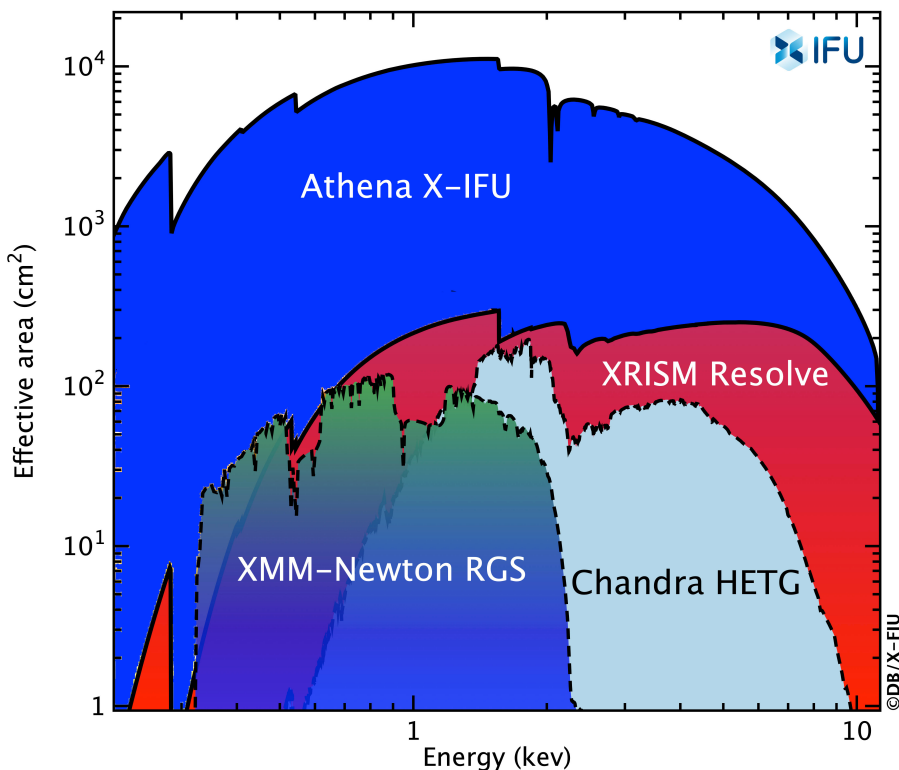
Figure 4.1: ATHENA X–IFU and XRISM Resolve calorimeters' effective areas shown along with dispersion spectrometers providing the largest A_e at the same band. The figure is a modified version of an X–IFU Consortium outreach illustration[a] comparing the A_e's of several instruments and concepts.

---

[a]https://www.the-athena-x-ray-observatory.eu/resources/gallery/x-ifu.html
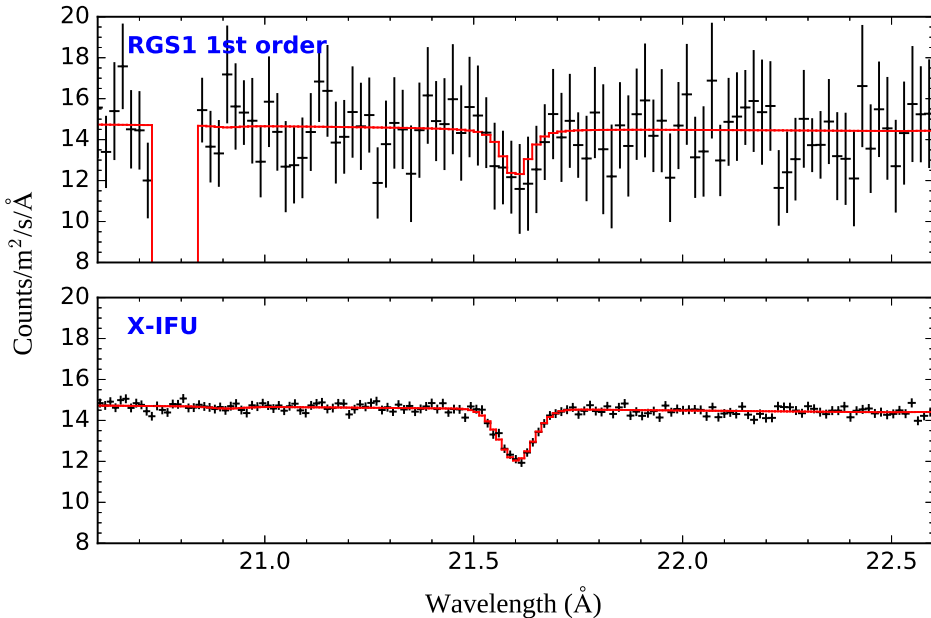
Figure 4.2: Simulated signal of Galactic O VII Heα absorption line in the X–ray continuum of quasar 3C 273. The simulative data corresponds that of 100 ks exposure time with XMM–Newton RGS1 (top panel) and Athena X–IFU (bottom panel). The red curve indicates the base–model (O VII –absorbed powerlaw) used in the the data simulation. The spectral data include 3 % Poissonian systematic error. The X–IFU response[a] is for baseline configuration. The RGS data was binned with a factor of 2, whereas the X–IFU data is plotted with the default bin sizes.

---

[a]http://x-ifu.irap.omp.eu/resources/for-the-community

5 From X-ray Measurements to Physical Interpretation

As discussed in the previous chapters, the signals of diffuse, X–ray emitting gas mediate the information on the physical environment of their origin. For istance, in a case of nearby, X–ray bright galaxy clusters and groups, the studies of high–resolution X–ray spectroscopy has enabled detailed information on the properties of the ICM/IGM, including those of temperature structure or velocity fields as we do in Papers IV and V. However, the situation is often different in other science cases, such as in WHIM studies, where the number and S/N of spectral lines are much lower. In such a case, the physical information obtainable through X–ray spectral analysis is limited. Yet even partial measurement information on X–ray absorbing/emitting gas can prove scientifically valuable when properly combined with complementary information available in FUV band (Sect. 5.1), and/or cosmological, hydrodynamical simulations (Sect. 5.2). In the following sections I discuss such methods from the perspective of WHIM studies.

5.1   Comparison to FUV Measurements

The UV–band contains the rest wavelengths of several metal ion transition lines whose abundancy peaks at the warm WHIM phase temperature range. These include, for instance, Ne VII, Ne VIII lines in EUV and O V, O VI in FUV. The most important spectral lines to study the warm WHIM phase are those produced by H I and O VI; H I Lyα (1215.7 Å), H I Lyβ (1025.7 Å), O VI Liα (1031.9 Å) and O VI Liβ (1037.6 Å). Given that an overwhelming majority of WHIM baryons are hydrogen, the H I Lyman alpha line finds use in detecting intergalactic absorbers and determining their redshifts accurately. This is particularly true in the warm phase regime, where observationally adequate fraction of hydrogen exist in neutral state. In addition to redshift data, the measurement limits on N_{HI} find use in constraining the

metallicity of the absorber in case where column density information of co–locating metal ions are available (provided that they belong to the same phase).

The high energy resolution power provided by FUV–band spectrometers enable direct measurements of spectral line–widths down to $b \approx 10 - 20$ km s^{-1}. This performance level is sufficient for measuring the velocity–distributions of strong warm(–hot) inter–galactic absorbers, as long as the gas is hot enough: at the lower boundary of WHIM, $T_i \approx 1 \times 10^5$ K, thermal broadening of oxygen lines is $b \approx 10$ km s^{-1}, whereas for hydrogen, it is $b \approx 40$ km s^{-1}. At present, FUV absorption studies have discovered numerous H I–O VI–absorbers from many AGN sight–lines, thereby opening the possibility to examine the incidence and characteristics of warm intergalactic absorbers with statistical methods [e.g, Savage et al., 2011, Tilton et al., 2012, Hussain et al., 2015, Pachat et al., 2016]. These studies have made it possible to make the first estimates on the amount of baryons in FUV detectable phases, as already presented earlier (in Fig. 1.2).

The X–ray band does not include hydrogen lines, but it does contain the major transition lines produced by the highest ionization level of oxygen (i.e., O VII and O VIII). Especially the O VII, being a subsequent ionic state to O VI, and possessing a high ionic fraction over a broad temperature range (see Fig. 5.1), stands out being a promising indicator for hot WHIM absorbers. In fact, the abundance of both of these ions peak at similar temperatures, and given the two orders of magnitude difference between the sensitivity of FUV/X–ray spectrometers, the absorbers with high enough O VII column densities to enable X–ray detection would be expected to be accompanied with FUV–detectable N_{OVI} in many cases.

The same is not true the other way around, and indeed, FUV band observations indicate that a large fraction of discovered intergalactic O VI absorbers must be at warm/cool temperatures (i.e., $T_i < 10^6$ K), namely due to their low b –parameter values. For instance, Tilton et al. [2012] examined a sample of 79 well–detected intergalactic O VI–absorbers and found a median b_{OVI}–parameter value of 27 km s^{-1} with 16 km s^{-1} standard deviation. However, as discussed in Paper I, such distributions may be biased towards lower b–values due to a selection effect; the detectability of a spectral line decreases as the b–parameter increases.

The effect of this selection effect might also be seen in Fig. 5.2, where I plot the b–parameters of 111 H I–O VI absorbers found in Tilton et al. [2012] sample. This sub–sample includes all the O VI absorbers with constrained linewidhts, i.e., those with $b_{OVI} > \Delta b_{OVI}$. In the figure, I plot the O VI b –parameters along with the b–parameters of the closest detected H I absorber (in terms of redshift), thus adopting an assumption that the detected signals originate from a common phase (i.e., $T_{OVI} = T_{HI}$). Should this be the case, then one would expect all the data points
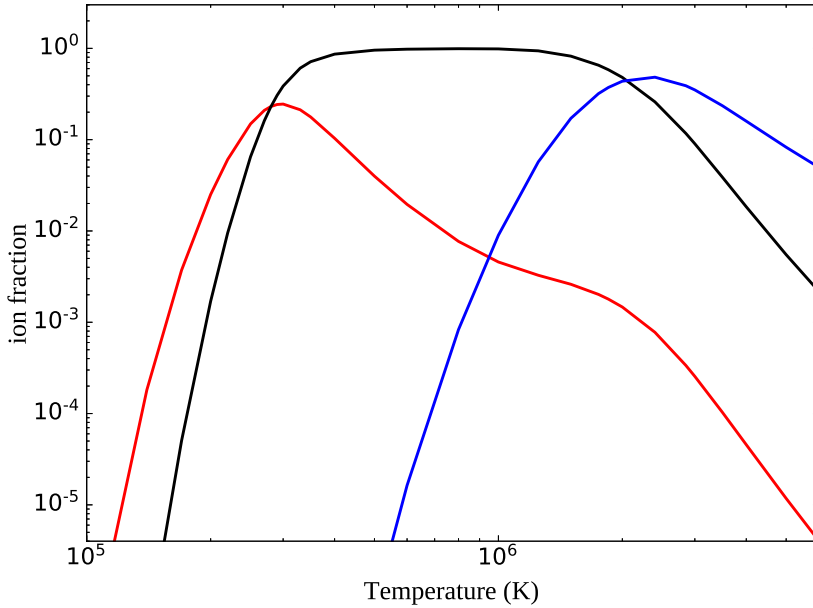
Figure 5.1: CIE ion fractions for oxygen at WHIM temperatures. The curves indicate the fractions for the most important oxygen ion species in WHIM: O VI(red), O VII(black) and O VIII(blue). Near the high temperature end of this figure ($T \gtrsim 3 \times 10^6$ K), the oxygen begins to get gradually fully ionized and becomes eventually undetectable.

to fall inside the white region of the figure, i.e., a region between the cases of thermal line–broadening only ($b_{non-th.} = 0$) and dominantly non–thermally broadened lines (so that $b_{th.} \ll b_{non-th}$ for both ions).

However, it can be seen, for instance, that $\approx 1/4$ of the data points fall outside the white region, indicating that the assumption of common phase is not the correct one for all the measurement points. Rather, it appears that the measurement data on O VI–rich phases' true H I counterparts are missing towards the broader O VI linewidths, perhaps due to complications in distuinquishing smeared BLA (broad Lyman alpha) lines from spectral data. Another eye–catching detail in the figure is, that $\approx 4/5$ of the data points indicate $T_i < 1.0 \times 10^5$ K, i.e., temperatures below the often quoted lower boundary of the WHIM temperature regime. In such a low temperatures, detection–enabling O VI ion columns cannot be produced by

collisional ionization mechanism, and therefore O VI would be likely produced via photo–ionization mechanism. I note that it is perfectly possible that a fraction of the broad O VI line detections are actually results of fits to non–resolvable blends of narrower O VI (or other) lines, which would bias the distribution by lifting such points upwards in the plane. However, it is also possible that the lines are inherently broad and miss–placed leftwards in the plane due to non–detection of their BLA counterparts. In that case the miss–placed data points (i.e., those falling on the top gray area) could indicate hot ion temperature. As can be seen from the figure, the hot phase oxygen ions' b parameters are always $\gtrsim 33$ km s^{-1}, translating into H I linewidts $b_{\text{HI}} \gtrsim 130$ km s^{-1}. Interestingly, there is only one such broad BLA detection in the whole 111 absorbers sample. I conclude this lengthy consideration of Fig. 5.2 by stressing the very special role of b–parameters in untackling some of the poorly understood aspects in WHIM science.

While broad O VI–absorbers can work as direct indicators of locations from where X–ray detectable O VII counterparts might be found, one should not focus only on broad FUV absorbers in the X–ray follow–up studies. Diffuse intergalactic gas structures, such as the IGM, ICM or WHIM, are expected to be thermally complex [see, e.g., McCabe et al., 2021, and the papers included in this thesis] and thus FUV established narrow O VI absorbers can work as sign–posts for hot O VII/O VIII absorbers just as well. Indeed, it is expected that the dominant ionization balance process behind intergalactic FUV–absorbers is photo–ionization, whereas detectable X–ray absorbers would more likely occur in denser environments where collisional ionization mechanism can dominate gas ionization state. If shock–heated gas in WHIM filaments has reached an equilibrium state, which is a reasonable assumption in case of X–ray detectable, high N_{OVII} hot WHIM absorbers [e.g., Fig 4 in Bykov et al., 2008], then its spectrum should be described well by the CIE model.

When this is the case, combining the information in X–ray and FUV data can yield relatively detailed information on the physical state of intergalactic absorbers with help of just a few line detections. As an example of this, let's consider a hypotetical, high quality X–ray detection of a hot CIE absorber characterized with prominent O VII Heα, O VII Heβ and O VIII Lyα lines. As discussed in this thesis, the X–ray analysis would, in such a case, enable one to constrain the temperature, oxygen ion fractions, the total oxygen column density, and (at least the lower limit on) oxygen Doppler spread parameter of the collisionally ionized gas phase. Therefore, the X–ray analysis would yield a direct prediction for spectral charasteristics of broad, hot–phase O VI lines present in the FUV band (N_{OVI}, and at least a lower limit on b_{OVI}). This information could be utilized as an input for more accurate FUV analysis of narrow O VI lines, for instance. Similarly, the X–ray constraints would

yield limits on b_{HI}, which would allow one to place limits on hot phase N_{HI} in FUV. The latter limits, in turn, could be used to constrain the gas metallicity of the X–ray absorbing CIE phase. In addition, I note that the CIE model predicts the line strengths for other elements as well, although this information depends also on the assumptions of the relative abundances of different elements. Given that the relative elemental abundances of metals are considered to be known with good accuracy, even non–detections of transition lines can be usefull in constraining the defining CIE model parameters (T, N_H) with increased accuracy (as we discuss in Paper II). It is noteworthy that in case of PIE, which is the expected ionization state for warm (narrow line) FUV absorbers, such predictions are not readily available but would need detailed information on the ionic number densities and the local radiation field at the location of the absorber. Therefore, to accurately estimate the total amount of oxygen and metallicity of WHIM absorbers, both X–ray and FUV constraints for different ion species are required. However, more sensitivite X–ray (and FUV) instruments are required to achieve this goal.

5.2   Comparison to Hydrodynamical Simulations

When analyzing the astronomical spectral data it is often the case that a large part of the signal of interest is hidden under the instrumental noise (i.e., line S/N< 1), and only the most prominent feature(s) can be detected and analyzed. Effectively this can hamper, or even prevent, the attempts to interpret the spectral signal appropriately. Observational WHIM research is an example of a topic where such additional information is essential, at least untill the era of the next generation instrumentation. One option to try to overcome this problem is to capitalize the information available from relevant simulations. In this section I discuss about some methods/findings that were used/obtained in the WHIM studies in Papers I-II.

   With current X–ray instumentation, the most robust observations of hot WHIM absorbers would consist of detection(s) of the strongest metal lines (such as O VII, O VIII, Ne IX or Ne X resonant lines) accompanying a well–detected intergalactic O VI–absorber. The FUV data, on the other hand, would typically yield limits on N_{OVI} and b_{OVI}, the latter of which gives the upper limit on the FUV detected phase ion temperature. If co–locating BLA would also be detected, then the limits for the FUV absorbing gas metallicity could also be constrained. The X–ray measurements, on the other hand, would give limits on the X–ray absorbing phase ion column densities, gas temperature, line broadening (i.e., T_{CIE} and/or a lower limit on b_{OVII}, T_{OVII} via the method described in Sect. 2.3.1), and possible predictions for FUV band as

described in Sect. 5.1. Combining all this information, one can examine whether the X–ray and FUV observations detect the same phase. Beyond that, there is only little usefull physical information that could be extracted from such measurement results (also given the rarity of the detected warm–hot systems). However, one can still take a few steps forward by capitalizing the information that is available from relevant physical simulations.

Cosmological, hydrodydamical simulations, such as the `EAGLE` [Schaye et al., 2015, Crain et al., 2015, McAlpine et al., 2016], IllustrisTNG [Nelson et al., 2019] or others, describe the evolution, properties and distribution of the galaxies, and that of the cosmic diffuse gas. In Papers I-II we took advantage of the `EAGLE` simulation data, so as to examine whether warm–hot absorbers like the ones considered in these papers do exist in `EAGLE`. As an example of this, in Fig. 5.3 I show the overall distribution of $N_{\rm OVI} - N_{\rm OVII}$ absorbers at $z = 0.1$ in `EAGLE` (gray histogram), along with those of hot (orange contours, absorbers with $T_{\rm ion} > 10^{6.1}$ K) and warm (blue contours, $T_{\rm ion} < 10^{6.1}$ K) gas phases. In the figure, the hot distribution encloses (roughly) a single phase CIE regime. Thus, beginning from the hot distribution and moving directly right–wards, one shifts to the parameter–space of cooler/multiphase gas. This part of the distribution follows roughly that of the warm gas in `EAGLE`. The figure gives us a map that can be used to examine what kind of counterparts one would expect to accompany any detection of either of the ions. For instance, one can see that any XMM–Newton RGS detectable O VII–absorber (upper green horizontal line) should be accompanied with detectable O VI ion column (green vertical line). However, as discussed, e.g., in Richter et al. [2008] (see also the discussions in Paper I), the FUV (O VI) line detectability depends also on b –parameter, so that the detectability of a line from an absorber with fixed ion column density decreases as the line gets broader. The figure also implies O VII to be more abundant ion than O VI in the `EAGLE` absorbers, which is an encouraging piece of information regarding to future X–ray missions that carry detectors that focus on hot WHIM observations (such as Athena X–IFU, see the lower horizontal line).

According to the `EAGLE` simulation, it appears likely that a large fraction of WHIM absorbers are multiphase, and that different ionization mechanisms can drive the ionization states of different gas phases that populate the same WHIM structure [Wijers et al., 2019]. In Fig. 5.4, I show an example of a comparison of our measurement results on sight–line towards blazar 3C 273 to `EAGLE` data. In this case, the X–ray and FUV analysis yielded a possible detection of a two–phase, warm–hot intergalactic absorber (Paper II). In the figure, we use measurement limits on column densities of four different ions to examine whether similar absorbers do exist in `EAGLE` data. We use our ion column density limits (measured separately for each ion) to

constrain the `EAGLE` data in T_{OVI}–T_{OVIII} -space, one ion at a time. It can be seen that while N_{OVI} and N_{OVII} do not have a big effect on the distribution, the limits on N_{OVIII} and N_{NeIX} cut the `EAGLE` distribution strongly. On top of the distribution, we plot the data point of a two–phase CIE model introduced in the paper, both of which were constrained with a use of stacked X–ray data (the warm phase CIE model was constrained by non–detections only, refer details in Paper II). Interestingly, the highly constrained `EAGLE` distribution matches our two–phase model which could indicate that our tentative detections reveal a spesific physical environment. However, a higher quality X–ray spectrum would be required to confirm the X–ray result, and to advance our understanding regarding to this absorber.
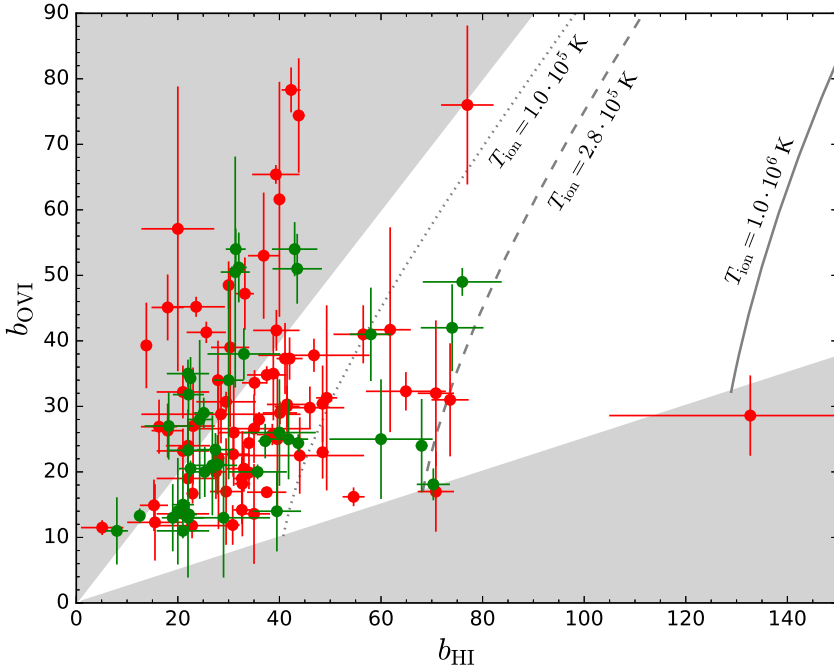
Figure 5.2: Measured linewidths of 111 H I–O VI-absorbers in the absorption sample presented in Table 4 of Tilton et al. [2012]. The white area indicates a parameter region where data points should fall when detecting the same gas phase. The lower boundary of this region corresponds to pure thermal line broadening, whereas the upper one indicates the limit where thermal broadening is negliglible compared to the non–thermal component. The curves show predicted relations between the two b–parameters at three different ion temperatures. From left to right, these correspond to: the nominal minimum temperature of the warm WHIM phase, CIE temperature where $f_{OVI} = f_{OVII}$, and the nominal temperature limit between the warm and hot WHIM phases. The H I–O VI absorbers with common redshifts are marked with green color, whereas the red circles mark the absorbers whose H I, O VI lines have a small z–offset ($\Delta z \lesssim 10^{-4}$). The error bars correspond to 1σ uncertainties.
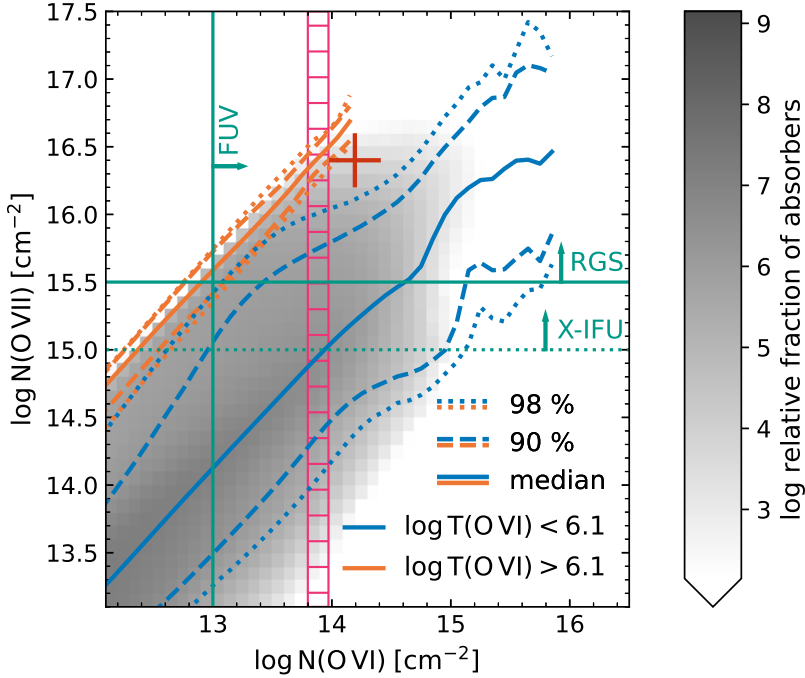
Figure 5.3: Ion column density distribution of co–located OVI and OVII in `EAGLE` (gray histogram in the background). The orange contours show the percentiles of N_{OVII} that are counterparts to OVI absorbers with mean ion-weighted OVI temperature $> 10^{6.1}$ K (hot phase) as a function of the total (i.e., for all phases) OVI column density. The blue contours show the same for $T_{\mathrm{OVI}} < 10^{6.1}$ K (warm phase). The green lines mark the approximate detection thresholds for OVI and OVII in FUV and X–ray bands. Detection thresholds for two representative X–ray instruments are shown: the RGS camera on–board *XMM–Newton*, and the Athena X-IFU. The distributions in this figure were constructed by examining the ion abundances in 3.125^2 kpc^2 sized, 6.25 cMpc deep rectangular boxes at 30000 `EAGLE` sight–lines [full details are described in Wijers et al., 2019].
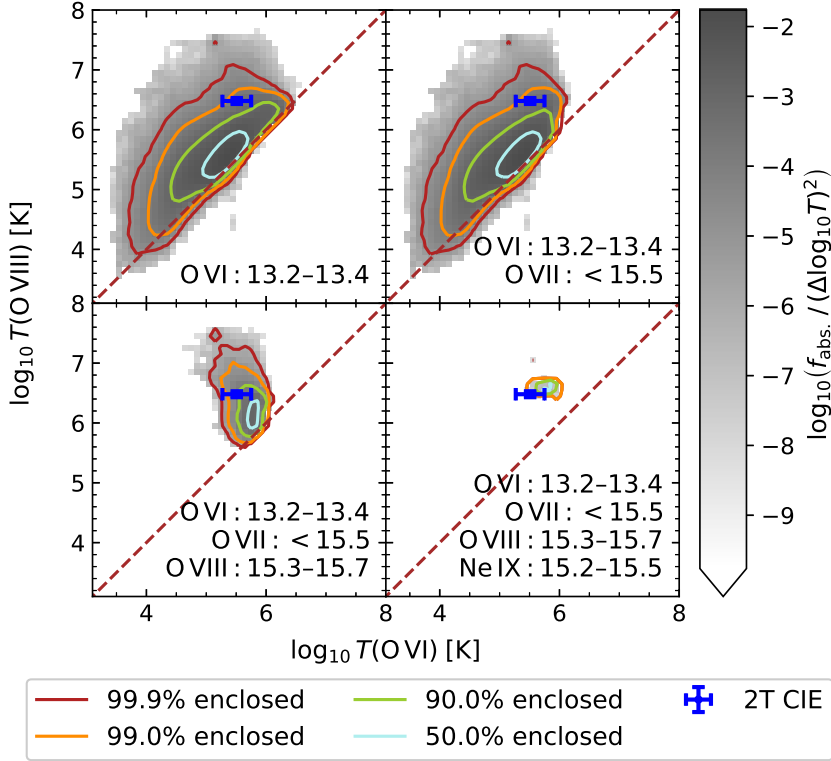
Figure 5.4: The distribution of O VI and O VII-weighted temperatures in counterparts to O VI absorbers (grayscale and contours) according to the EAGLE simulation, compared to the best-fit temperatures at $z = 0.09$ for the 2-temperature CIE model (warm and hot phase, respectively) as presented in Ahoranta et al. [2019]. From left to right, top to bottom, we show how constraints on the column densities of different ions affect the temperatures of O VI and O VIII absorbers in EAGLE. Column density ranges are shown in units of $\log_{10}$ cm^{-2} for the different ions. The O VI constraints are from Tilton et al. [2012]. The contours enclose different fractions of the absorbers in each column density selection, as indicated in the legend, while the grayscale shows the fraction of all EAGLE absorbers satisfying the indicated constraints. The dashed line indicates where the temperatures are equal. Most absorbers are multiphase and the 2T CIE model is consistent with EAGLE.

6 Summary of the publications

The thesis consists of five refereed publications that are listed below in reverse chronological order:

- **Paper I: J. Ahoranta**, A. Finoguenov, M. Bonamente, S. Muzahid, N. Wijers, E. Tilton and J. Schaye, *Discovery of a multiphase O VI and O VII absorber in the circumgalactic/intergalactic transition region*, A&A, vol. 656, pp. A107, December 2021

- **Paper II: J. Ahoranta**, J. Nevalainen, N. Wijers, A. Finoguenov, M. Bonamente, E. Tempel, E. Tilton, J. Schaye, J. S. Kaastra and G. Gozaliasl, *Hot WHIM counterparts of FUV O VI absorbers: Evidence in the line-of-sight towards quasar 3C 273*, A&A, vol. 634, pp. A106, February 2020

- **Paper III:** J. Nevalainen, E. Tempel, **J. Ahoranta**, L. J Liivamägi, M. Bonamente, E. Tilton, J. S. Kaastra, T. Fang, P. Heinämäki, E. Saar and A. Finoguenov, *To be or not to be: the case of the hot WHIM absorption in the blazar PKS 2155-304 sight line*, A&A, vol. 621, pp. A88, January 2019

- **Paper IV: J. Ahoranta**, A. Finoguenov, C. Pinto, J. S Sanders, J. S Kaastra, J. de Plaa and A. C. Fabian, *Observations of asymmetric velocity fields and gas cooling in the NGC 4636 galaxy group X-ray halo*, A&A, vol. 592, pp. A145, August 2016

- **Paper V:** C. Pinto, A. C. Fabian, N. Werner, P. Kosec, **J. Ahoranta**, J. de Plaa, J. S. Kaastra, J. S. Sanders, Y. Y. Zhang and A. Finoguenov, *Discovery of O VII line emitting gas in elliptical galaxies*, A&A, vol. 572, pp. L8, December 2014

In the next sections I give brief summaries of each of the publications listed above. My contribution to the papers is described at the end of each section.

6.1   Paper I

Paper I: (Ahoranta, Finoguenov, Bonamente et al. 2021)
Summary:
The paper presents an X–ray follow–up study on intergalactic FUV O VI –absorber
in the sight–line towards Seyfert I galaxy Ton S180. We measure O VII –absorption
at $\sim 5\sigma$ confidence level at a redshift matching that of the established O VI absorber
at $z \approx 0.0456$. A detailed re–analysis of FUV data indicates a total of three metal
absorbers within $\approx 70\ \mathrm{km\,s^{-1}}$ in respect to the O VII absorber redshift. We introduce
an analysis method, based on the line saturation effect, which allows us to constrain
the lower limit on O VII b –parameter. Applying this method excludes the possibility
that the FUV and X–ray observations detect a common absorbing gas phase with
$> 90\ \%$ confidence level, thus implying that the O VI–O VII absorbing medium is in
multiphase state. We analyze the galactic environment in the vicinity of the absorber
and find the sight–line to pass through a filamentary distribution of galaxies, three
of which locate ≈ 2 to $3\ r_{200}$ distance from the sight–line. We interpret that the
measurements trace gas within circumgalactic/intergalactic transition region, and
find that the measured N_{OVII} is by a factor of two further away from the nearest
detected galaxies compared to the case with similar absorbers in `EAGLE`. We consider
b –parameters effect on line detectability in FUV and X–ray spectral data and find
that FUV band instruments are more sensitive to narrow lines, whereas the opposite
is true in the X–ray band. We conclude that such behaviour of line detectability
reduces the probability to detect the true O VII counterparts to FUV detected O VI,
and vice versa. The paper highlights the crucial role of linewidth measurements in
the WHIM research.

Author's contribution: All the analysis excluding FUV spectral fitting and
`EAGLE` analysis. Development of new analysis methods that allowed us to reach our
main conclusions. Main responsibility of writing the manuscript.

6.2   Paper II

Paper II: (Ahoranta, Nevalainen, Wijers et al. 2020)
Summary: The paper presents an X–ray follow–up study on intergalactic FUV O VI
–absorbers in the line of sight towards quasar 3C 273. We examine the absorption
imprints in X–ray spectra at the redshifts of two established FUV O VI –absorbers
in this sight–line, found at redshifts 0.09 and 0.12. While the latter redshift gives us

a non–detection, we find evidence of Ne IX and O VIII ion absorption at $z_{\mathrm{OVI}} \approx 0.09$. The O VII absorption cannot be studied in detail at this redshift due to incidental line blending of O VII Heα with Galactic O I doublet. Fitting a CIE absorption model to X–ray data constraints the gas temperature to $kT = 0.26 \pm 0.03$ keV (i.e., $T_{\mathrm{X-ray}} \approx 3\times10^6$ K), while producing Ne IX and O VIII absorption consistent with that measured separately from the line fluxes in the spectral data. In contrast, we constrain the FUV absorbing phase's temperature to $T_{\mathrm{FUV}} \approx 3\times10^5$ K, which implies a multiphase structure for the $z = 0.09$ absorber. We find our two–temperauture solution to match the `EAGLE` prediction for the absorbers that are characterized with similar ion column densities than the measured ones (i.e., N_{OVI}, N_{OVIII}, N_{NeIX} and upper limit on N_{OVII}). We link the absorption to a filamentary concentration of galaxies, which we detect by analyzing the SDSS galaxy distribution data with the Bisous model. This article aims to demonstrate X–ray band follow–up studies' (on FUV established O VI absorbers) applicability in studying the warm–hot WHIM aborbers with future X–ray instruments, such as the XRISM and Athena X–IFU.

Author's contribution: All the analysis excluding the `EAGLE` analysis and Bisous modeling. Development of some new analysis techiques usefull in WHIM research. Main responsibility of writing the manuscript. Presenting the work in international conferences.

6.3 Paper III

Paper III: (Nevalainen, Tempel, Ahoranta et al. 2019)
Summary: The paper presents an X–ray follow–up study considering six intergalactic FUV absorbers (BLA, O VI, Si IV) in a sight–line towards blazar PKS 2155-304. This line–of–sight has special interest, as it includes a previously published X–ray line detection at $\lambda \approx 20$ mA (Chandra LETG ACIS detection), interpreted as O VIII Lyα line co–locating FUV detected O VI absorber detected at $z_{\mathrm{OVI}} \approx 0.054$. In the paper, we consider all the available high energy resolution data measured towards the PKS 2155-304. This includes 1200 ks worth of XMM–Newton RGS spectral data (only 1st spectral order is considered), 330 ks Chandra LETG ACIS data (we consider both plus and minus orders) and 310 ks LETG HRC data (plus and minus orders). Analyzing this data, while looking for possible O VII/O VIII absorption signals at the 6 FUV redshifts, gives us a non–detection elsewhere but at $z_{\mathrm{OVI}} \approx 0.054$. We therefore focus on examining the previously detected O VIII Lyα signal at $z_{\mathrm{OVI}} \approx 0.054$, but find that the line–feature occurs only in LETG ACIS data. Given that both the LETG+HRC combination, and the exceptionally high quality XMM–Newton RGS1

data misses to detect this line, we conclude that the previous interpretation for the ACIS detected line is unlikely (99.994 % confidence level) correct.

Author's contribution: Preparing the XMM–Newton RGS and Chandra LETG+ACIS/HRC spectra that are considered in the paper. Conducting simultanous spectral analysis of the set of 25 individual RGS 1st order spectra to confirm the XMM–Newton non–detection was not due to overlooked complications in co–addition process (Sect. 4.3.1.). Commenting on the prepared manuscript.

6.4 Paper IV

Paper IV: (Ahoranta, Finoguenov, Pinto et al. 2016)
Summary: In this paper we publish a detailed analysis on the properties of X–ray emitting gas at the central regions of the NGC 4636 galaxy group. The IGM at the center of the group is notably disturbed, including X–ray cavities presumably due to previous AGN outbursts from the central galaxy to the surrounding medium. Our paper presents one–dimensional (cross–dispersion direction) radial analysis of XMM–Newton RGS data on this source, along with complementary, two–dimensional analysis of Chandra ACIS imaging spectrometer data. The high–resolution analysis confirms previously published Fe XVII resonant line scattering (i.e., $[I_{\lambda 17.05} + I_{\lambda 17.10}]/I_{\lambda 15.01}$) at the peak of the X–ray emission, but the radial analysis in (approximate) north–south direction revealed an off–set between the distributions of resonant scattering and the X–ray emission. Specifically, our analysis indicates strong Fe XVII resonant scattering from center to north, while it is completely absent at the south side. Similarly, spectral modeling indicates surpressed cooling flow rate at the south side. Examination of RGS–extraction–scheme–corresponding spectral regions with Chandra data, but dividing these regions into eastern and western sectors, suggests a presence of cool, $kT \approx 0.3 - 0.4$ keV gas phases at the center and in the western sectors at the north side. No indication of such cool gas was obtained in the spectral regions of the south side, where the scatter of thermal phases appeared to be generally smaller. The presented 2D–maps imply core sloshing motion towards (approximately) north–east direction on the skyplane, as indicated by a tail of cooled gas ($kT \approx 0.6 - 0.8$ keV) that stretches towards the opposite direction. In the paper we consider three different scenarios that could explain our result.

Author's contribution: All the analysis except the preparation of the 2D spectral maps. Realization of the 1D analysis method for XMM-Newton RGS data (in collaboration with Dr. C.Pinto). Main responsibility of writing the manuscript. Presenting the results in international conference.

6.5   Paper V

Paper V: (Pinto, Fabian, Werner et al. 2014):

Summary: In this editorial letter we publish discovery of cool, $kT < 0.5$ keV gas in the core regions of six individual cool core galaxy groups, and around three individual galaxies that are members of the Virgo Cluster. We analyze deep XMM–Newton RGS observations of these sources to study Fe XVII and O VII emission, the latter of which had only detected in co-added spectra combining the data of numerous different cool core systems ($kT < 1$ keV) at the time. In the paper, we detect both Fe XVII and O VII (resonant and forbidden) emission lines at each of the nine sources. We analyze resonant line scattering of both of the ions, and estimate cooling flow rates at each of the individual object. In general, the analysis yielded cooling flow rates $\dot{M} \approx 0.2 - 1.8 \ M_\odot \, \mathrm{yr}^{-1}$ and indicatons of resonant scattering of both the ions in all objects. However, due to the insufficient spectral photon statistics, we were not able to solve whether the Fe XVII and O VII trace the same cooled gas phase in this paper.

Author's contribution: Analysis and discovery of O VII emission lines in the cool core of the NGC 4636 galaxy group previously concluded to be absent in literature. Participation in manuscript preparation along with the other authors.

7 Concluding remarks

Our understanding on abundance, distribution and properties of hot, highly ionized cosmic baryons has progressed significantly during the past few decades. On one hand, this has been accomplished through the use of improved X—ray and UV instrumentation that has produced more accurate measurement data at higher sensitivity level than before. On the other hand, our theoretical understanding has advanced substantially owing to the development of sophisticated cosmological, hydrodynamical simulations. These two distinct sources of information, and the interplay between them, provide the building blocks needed in constructing our understanding on the cosmic large scales structures.

In this thesis, the focus lies on observational research of hot ($\gtrsim 10^6$ K), intergalactic gas. Due to practical reasons, this sector presents (presumably) the most juvenile research branch when it comes to studying the cosmic baryons. But at the same time, it has the potential to be the most fruitful one, given the large fraction of (undetected) cosmic baryons that we expect to exist in this state.

The research papers included in this work represent our endeavors to contribute to the progress of understanding the distribution, properties and states of hot, cosmic baryons. A lot of this work is based on extensive familiarization to existing archival data, and on seeking and developing analysis methods capable to extract information embedded in data to the fullest extent. I present high energy resolution studies examining thermal and dynamical structures of intergalactic gas in galaxy group/cluster environment, and papers on newly discovered hot intergalactic absorbers along with general discussions regarding to the observability of the WHIM.

The future of observational X–ray astronomy looks bright: novel micro–calorimeter technology promises new X–ray instruments capable in spatial, high energy resolution observations at unforeseen sensitivity level. The transition to the new observational era is close, as the launch of XRISM telescope approaches. But the crown jewel of future X–ray astronomy, the Athena space telescope, will let us await for another decade.

The X–IFU instrument technological development is currently ongoing, and Finland (including myself) has a part in this work. In that regard, any new observational information in X–IFU's science fields is now in high value, as there is still a possibility to influence on the final instrument concept. The main motivation behind this PhD research was to produce such information.

7 Bibliography

J. Ahoranta, J. Nevalainen, N. Wijers, A. Finoguenov, et al. *Astronomy & Astrophysics*, 634:A106, 2019. doi: 10.1051/0004-6361/201935846.

J. Ahoranta, A. Finoguenov, M. Bonamente, E. Tilton, N. Wijers, S. Muzahid, and J. Schaye. Discovery of a multiphase OVI and OVII absorber in the circumgalactic/intergalactic transition region. *arXiv e-prints*, art. arXiv:2109.12146, September 2021.

Jussi Ahoranta, Alexis Finoguenov, Ciro Pinto, Jeremy Sanders, Jelle Kaastra, Jelle de Plaa, and Andrew Fabian. Observations of asymmetric velocity fields and gas cooling in the NGC 4636 galaxy group X-ray halo. *Astronomy & Astrophysics*, 592:A145, August 2016. doi: 10.1051/0004-6361/201527523.

R. Bacon, D. Mary, T. Garel, J. Blaizot, M. Maseda, J. Schaye, L. Wisotzki, S. Conseil, J. Brinchmann, F. Leclercq, V. Abril-Melgarejo, L. Boogaard, N. F. Bouché, T. Contini, A. Feltre, B. Guiderdoni, C. Herenz, W. Kollatschny, H. Kusakabe, J. Matthee, L. Michel-Dansac, T. Nanayakkara, J. Richard, M. Roth, K. B. Schmidt, M. Steinmetz, L. Tresse, T. Urrutia, A. Verhamme, P. M. Weilbacher, J. Zabl, and S. L. Zoutendijk. The MUSE Extremely Deep Field: The cosmic web in emission at high redshift. *Astronomy & Astrophysics*, 647:A107, March 2021. doi: 10.1051/0004-6361/202039887.

D. Barret, T. Lam Trong, J. W. den Herder, et al. *Space Telescopes and Instrumentation2016: Ultraviolet to Gamma Ray*, 9905:99052F, 2016.

M. Bonamente, J. Nevalainen, E. Tilton, J. Liivamagi, E. Tempel, P. Heinamaki, and Fang. T. *Monthly Notices of the Royal Astronomical Society*, 457:4236, 2016.

A. M. Bykov, F. B. S. Paerels, and V. Petrosian. *Space Sci Rev*, 134:141, 2008.

R. Cen and J. P. Ostriker. *The Astrophysical Journal*, 514:1, 1999.

S. M. Chung, J. J. Drake, V. L. Kashyap, P. W. Ratzlaff, and B. J. Wargelin. Characterizing nonlinearities in the chandra letg+hrc-s dispersion relation. *Proc. SPIE*, 5488:12, Oct 2004. doi: 0.1117/12.55219. URL https://doi.org/10.1117/12.552194.

R. A. Crain, J. Schaye, R. G. Bower, M. Furlong, M. Schaller, T. Theuns, C. Dalla Vecchia, C. S. Frenk, I. G. McCarthy, J. C. Helly, A. Jenkins, Y. M. Rosas-Guevara, S. D. M. White, and J. W. Trayford. *Monthly Notices of the Royal Astronomical Society*, 450:1937–1961, 2015.

Romeel Davé, Renyue Cen, Jeremiah P. Ostriker, Greg L. Bryan, Lars Hernquist, Neal Katz, David H. Weinberg, Michael L. Norman, and Brian O'Shea. Baryons in the Warm-Hot Intergalactic Medium. *The Astrophysical Journal*, 552(2):473–483, May 2001. doi: 10.1086/320548.

J. de Plaa, J. S. Kaastra, N. Werner, C. Pinto, P. Kosec, Y. Y. Zhang, F. Mernier, L. Lovisari, H. Akamatsu, G. Schellenberger, F. Hofmann, T. H. Reiprich, A. Finoguenov, J. Ahoranta, J. S. Sanders, A. C. Fabian, O. Pols, A. Simionescu, J. Vink, and H. Böhringer. CHEERS: The chemical evolution RGS sample. *Astronomy & Astrophysics*, 607:A98, November 2017. doi: 10.1051/0004-6361/201629926.

R. Doron and E. Behar. *ApJ*, 574:518–526, 2002.

T. Fang, J. Bullock, and M. Boylan-Kolchin. *The Astrophysical Journal*, 762:20, 2012.

U. Fano. Ionization yield of radiations. ii. the fluctuations of the number of ions. *Phys. Rev.*, 72:26–29, Jul 1947. doi: 10.1103/PhysRev.72.26. URL https://link.aps.org/doi/10.1103/PhysRev.72.26.

III Gott, J. Richard, Adrian L. Melott, and Mark Dickinson. The Sponge-like Topology of Large-Scale Structure in the Universe. *The Astrophysical Journal*, 306:341, July 1986. doi: 10.1086/164347.

T. Hussain, S. Muzahid, A. Narayanan, R. Srianand, B. P. Wakker, J. C. Charlton, and A. Pathak. HST/COS detection of a Ne VIII absorber towards PG 1407+265: an unambiguous tracer of collisionally ionized hot gas? *Monthly Notices of the Royal Astronomical Society*, 446(3):2444–2455, Jan 2015. doi: 10.1093/mnras/stu2285.

J. S. Kaastra, R. Mewe, and H. Nieuwenhuijzen. SPEX: a new code for spectral analysis of X UV spectra. In K. Yamashita and T. Watanabe, editors, *UV and X-ray Spectroscopy of Astrophysical and Laboratory Plasmas*, pages 411–414, 1996.

J. S. Kaastra, C. P. de Vries, K. C. Steenbrugge, et al. *Astronomy & Astrophysics*, 534:37, 2011.

J. S. Kaastra, A. J. J. Raassen, J. de Plaa, and Liyi Gu. Spex x-ray spectral fitting package. Zenodo, December 2018. URL https://doi.org/10.5281/zenodo.2419563. 10.5281/zenodo.2419563.

Jelle Kaastra, Alexis Finoguenov, Fabrizio Nicastro, Enzo Branchini, Joop Schaye, Nico Cappelluti, Jukka Nevalainen, Xavier Barcons, Joel Bregman, Judith Croston, Klaus Dolag, Stefano Ettori, Massimiliano Galeazzi, Takaya Ohashi, Luigi Piro, Etienne Pointecouteau, Gabriel Pratt, Thomas Reiprich, Mauro Roncarelli, Jeremy Sanders, Yoh Takei, and Eugenio Ursino. The Hot and Energetic Universe: The missing baryons and the warm-hot intergalactic medium. *arXiv e-prints*, art. arXiv:1306.2324, June 2013.

O. E. Kovacs, A. Bogdan, R. K. Smith, R. P. Kraft, and W. R. Forman. *The Astrophysical Journal*, 872:83, 2019.

S. D. Loch, M. S. Pindzola, C. P. Ballance, and D. C. Griffin. *J. Phys. B: At. Mol. Opt. Phys.*, 39:85, 2006.

J. P. Macquart, J. X. Prochaska, M. McQuinn, K. W. Bannister, S. Bhandari, C. K. Day, A. T. Deller, R. D. Ekers, C. W. James, L. Marnoch, S. Osłowski, C. Phillips, S. D. Ryder, D. R. Scott, R. M. Shannon, and N. Tejos. A census of baryons in the Universe from localized fast radio bursts. , 581(7809):391–395, May 2020. doi: 10.1038/s41586-020-2300-2.

D. Martizzi, M. Vogelsberger, M. C. Artale, M Haider, et al. *MNRAS*, 486:3766–3787, 2019.

S. McAlpine, J. C. Helly, M. Schaller, J. W. Trayford, Y. Qu, et al. *Astronomy and Computing*, 15:72–89, 2016.

Tyler McCabe, Sanchayeeta Borthakur, Timothy Heckman, Jason Tumlinson, Rongmon Bordoloi, and Romeel Dave. Detection of a Multiphase Intragroup Medium: Results from the COS-IGrM Survey. *The Astrophysical Journal*, 923(2):189, December 2021. doi: 10.3847/1538-4357/ac283c.

F. Mernier, V. Biffi, H. Yamaguchi, P. Medvedev, A. Simionescu, S. Ettori, N. Werner, J. S. Kaastra, J. de Plaa, and L. Gu. Enrichment of the Hot Intracluster Medium: Observations. , 214(8):129, December 2018. doi: 10.1007/s11214-018-0565-7.

R. Mewe, E. H. B. M. Gronenschild, and G. H. J. van den Oord. Calculated X-Radiation from Optically Thin Plasmas - Part Five. *Astronomy & Astrophysics Supplement Series*, 62:197, November 1985.

R. Mewe, J. R. Lemen, and G. H. J. van den Oord. Calculated X-radiation from optically thin plasmas. VI - Improved calculations for continuum emission and approximation formulae for nonrelativistic average Gaunt actors. *Astronomy & Astrophysics Supplement Series*, 65:511–536, September 1986.

Julio F. Navarro, Carlos S. Frenk, and Simon D. M. White. The structure of cold dark matter halos. *The Astrophysical Journal*, 462:563, May 1996. ISSN 1538-4357. doi: 10.1086/177173. URL http://dx.doi.org/10.1086/177173.

Dylan Nelson, Volker Springel, Annalisa Pillepich, Vicente Rodriguez-Gomez, Paul Torrey, Shy Genel, Mark Vogelsberger, Ruediger Pakmor, Federico Marinacci, Rainer Weinberger, Luke Kelley, Mark Lovell, Benedikt Diemer, and Lars Hernquist. The IllustrisTNG simulations: public data release. *Computational Astrophysics and Cosmology*, 6(1):2, May 2019. doi: 10.1186/s40668-019-0028-x.

N. Nelson, G. Kauffmann, A. Pillepich, et al. *arxiv:1712.00016*, 2018.

F. Nicastro, J. Kaastra, Y. Krongold, S. Borgani, E. Branchini, R. Cen, M. Danina, et al. *Nature*, 558:406, 2018.

Donald E. Osterbrock. *Astrophysics of gaseous nebulae.* 1974.

Sachin Pachat, Anand Narayanan, Sowgat Muzahid, Vikram Khaire, Raghunathan Srianand, Bart P. Wakker, and Blair D. Savage. A pair of O VI and broad Ly α absorbers probing warm gas in a galaxy group environment at z 0.4. *Monthly Notices of the Royal Astronomical Society*, 458(1):733–746, May 2016. doi: 10.1093/mnras/stw194.

Steven V. Penton, J. Michael Shull, and John T. Stocke. The Local Lyα Forest. II. Distribution of H I Absorbers,Doppler Widths, and Baryon Content. *The Astrophysical Journal*, 544(1):150–175, November 2000. doi: 10.1086/317179.

S. Perlmutter, G. Aldering, G. Goldhaber, R. A. Knop, P. Nugent, P. G. Castro, S. Deustua, S. Fabbro, A. Goobar, D. E. Groom, I. M. Hook, A. G. Kim, M. Y. Kim, J. C. Lee, N. J. Nunes, R. Pain, C. R. Pennypacker, R. Quimby, C. Lidman, R. S. Ellis, M. Irwin, R. G. McMahon, P. Ruiz-Lapuente, N. Walton, B. Schaefer, B. J. Boyle, A. V. Filippenko, T. Matheson, A. S. Fruchter, N. Panagia, H. J. M. Newberg, W. J. Couch, and The Supernova Cosmology Project. Measurements of Ω and Λ from 42 High-Redshift Supernovae. *The Astrophysical Journal*, 517(2): 565–586, June 1999. doi: 10.1086/307221.

Ciro Pinto, Jeremy S. Sanders, Norbert Werner, Jelle de Plaa, Andrew C. Fabian, Yu-Ying Zhang, Jelle S. Kaastra, Alexis Finoguenov, and Jussi Ahoranta. Chemical Enrichment RGS cluster Sample (CHEERS): Constraints on turbulence. *Astronomy & Astrophysics*, 575:A38, March 2015. doi: 10.1051/0004-6361/201425278.

Planck Collaboration, P. A. R. Ade, N. Aghanim, M. I. R. Alves, C. Armitage-Caplan, M. Arnaud, M. Ashdown, F. Atrio-Barandela, J. Aumont, H. Aussel, and et al. *Astronomy & Astrophysics*, 571:A1, 2014.

P. Richter, F. B. S. Paerels, and J. S. Kaastra. *Space Sci.Rev.*, 134:25, 2008.

Adam G. Riess, Alexei V. Filippenko, Peter Challis, Alejandro Clocchiatti, Alan Diercks, Peter M. Garnavich, Ron L. Gilliland, Craig J. Hogan, Saurabh Jha, Robert P. Kirshner, B. Leibundgut, M. M. Phillips, David Reiss, Brian P. Schmidt, Robert A. Schommer, R. Chris Smith, J. Spyromilio, Christopher Stubbs, Nicholas B. Suntzeff, and John Tonry. Observational Evidence from Supernovae for an Accelerating Universe and a Cosmological Constant. *The Astronomical Journal*, 116 (3):1009–1038, September 1998. doi: 10.1086/300499.

B. D. Savage, N. Lehner, and A. Narayanan. COS Observations of Metal Line and Broad Lyman-α Absorption in the Multi-phase O VI and Ne VIII System at z = 0.20701 toward HE 0226-4110. *The Astrophysical Journal*, 743(2):180, Dec 2011. doi: 10.1088/0004-637X/743/2/180.

J. Schaye, R. A. Crain, R. G. Bower, M. Furlong, et al. *Monthly Notices of the Royal Astronomical Society*, 446:521, 2015.

Uro š Seljak, Alexey Makarov, Patrick McDonald, Scott F. Anderson, Neta A. Bahcall, J. Brinkmann, Scott Burles, Renyue Cen, Mamoru Doi, James E. Gunn, Željko Ivezić, Stephen Kent, Jon Loveday, Robert H. Lupton, Jeffrey A. Munn, Robert C. Nichol, Jeremiah P. Ostriker, David J. Schlegel, Donald P. Schneider, Max Tegmark, Daniel E. Vanden Berk, David H. Weinberg, and Donald G.

York. Cosmological parameter analysis including sdss lyα forest and galaxy bias: Constraints on the primordial spectrum of fluctuations, neutrino mass, and dark energy. *Phys. Rev. D*, 71:103515, May 2005. doi: 10.1103/PhysRevD.71.103515. URL `https://link.aps.org/doi/10.1103/PhysRevD.71.103515`.

Michael Shull, Britton Smith, and Charles Danforth. The baryon census in a multiphase intergalactic medium: 30% of the baryons may still be missing. *Astrophysical Journal*, 759, 12 2011. doi: 10.1088/0004-637X/759/1/23.

Tadayuki Takahashi, Kazuhisa Mitsuda, Richard Kelley, and et al. The ASTRO-h x-ray astronomy satellite. In Tadayuki Takahashi, Jan-Willem A. den Herder, and Mark Bautz, editors, *SPIE Proceedings*. SPIE, jul 2014. doi: 10.1117/12.2055681. URL `https://doi.org/10.1117%2F12.2055681`.

E. Tilton, C. W. Danforth, M. J Shull, and T. L. Ross. *The Astrophysical Journal*, 759:112, 2012.

T. Tuominen, J. Nevalainen, E. Tempel, T. Kuutma, N. Wijers, J. Schaye, P. Heinämäki, M. Bonamente, and P. Ganeshaiah Veena. An EAGLE view of the missing baryons. *Astronomy &amp Astrophysics*, 646:A156, feb 2021. doi: 10.1051/0004-6361/202039221. URL `https://doi.org/10.1051%2F0004-6361%2F202039221`.

H. Umehata, M. Fumagalli, I. Smail, Y. Matsuda, A. M. Swinbank, S. Cantalupo, C. Sykes, R. J. Ivison, C. C. Steidel, A. E. Shapley, J. Vernet, T. Yamada, Y. Tamura, M. Kubo, K. Nakanishi, M. Kajisawa, B. Hatsukade, and K. Kohno. Gas filaments of the cosmic web located around active galaxies in a protocluster. *Science*, 366(6461):97–100, October 2019. doi: 10.1126/science.aaw5949.

L. M. Voigt and A. C. Fabian. Galaxy cluster mass profiles. *Monthly Notices of the Royal Astronomical Society*, 368(2):518–533, May 2006. ISSN 1365-2966. doi: 10.1111/j.1365-2966.2006.10199.x. URL `http://dx.doi.org/10.1111/j.1365-2966.2006.10199.x`.

N. Wijers, J. Schaye, B. D. Oppenheimer, R. A. Crain, and F. Nicastro. *Monthly Notices of the Royal Astronomical Society*, 2019.

XRISM Science Team. Science with the X-ray Imaging and Spectroscopy Mission (XRISM). *arXiv e-prints*, art. arXiv:2003.04962, March 2020.